BASS. XXIX. The near-infrared view of the broad-line region (BLR) the effects of obscuration in BLR characterization

Ricci, F.; Treister, E.; Bauer, F.E.; Mejía-Restrepo, J.E.; Koss, M.J.; den Brok, J.S.; ... ; Veilleux, S.

Note: To cite this publication please use the final published version (if applicable).

BASS. XXIX. The Near-infrared View of the Broad-line Region (BLR): The Effects of Obscuration in BLR Characterization[*]

Federica Ricci[1,2,3,4], Ezequiel Treister[1], Franz E. Bauer[1,5,6], Julian E. Mejía-Restrepo[7], Michael J. Koss[8],
Jakob S. den Brok[9,10], Mislav Baloković[11,12,13], Rudolf Bär[9], Patricia Bessiere[14], Turgay Caglar[15], Fiona Harrison[16],
Kohei Ichikawa[17], Darshan Kakkad[7], Isabella Lamperti[18,19,20], Richard Mushotzky[21], Kyuseok Oh[22,23,35],
Meredith C. Powell[24], George C. Privon[25,26], Claudio Ricci[27,28,29], Rogerio Riffel[30], Alejandra F. Rojas[31],
Eleonora Sani[7], Krista L. Smith[32], Daniel Stern[33], Benny Trakhtenbrot[34], C. Megan Urry[13], and Sylvain Veilleux[21]

[1] Instituto de Astrofísica and Centro de Astroingeniería, Facultad de Física, Pontificia Universidad Católica de Chile, Casilla 306, Santiago 22, Chile
federica.ricci@uniroma3.it
[2] Dipartimento di Fisica e Astronomia, Università di Bologna, via Gobetti 93/2, I-40129 Bologna, Italy
[3] INAF—Osservatorio di Astrofisica e Scienza dello Spazio di Bologna, via Gobetti 93/3, I-40129 Bologna, Italy
[4] Dipartimento di Matematica e Fisica, Università Roma Tre, via della Vasca Navale 84, I-00146, Roma, Italy
[5] Millennium Institute of Astrophysics (MAS), Nuncio Monseñor Sótero Sanz 100, Providencia, Santiago, Chile
[6] Space Science Institute, 4750 Walnut Street, Suite 205, Boulder, CO 80301, USA
[7] European Southern Observatory, Alonso de Cordova 3107, Vitacura, Casilla 19001, Santiago de Chile, Chile
[8] Eureka Scientific, 2452 Delmer Street, Suite 100, Oakland, CA 94602-3017, USA
[9] Institute for Particle Physics and Astrophysics, ETH Zürich, Wolfgang-Pauli-Strasse 27, CH-8093 Zürich, Switzerland
[10] Argelander Institute for Astronomy, Auf dem Hügel 71, D-53231, Bonn, Germany
[11] Center for Astrophysics, Harvard & Smithsonian, 60 Garden Street, Cambridge, MA 02138, USA
[12] Black Hole Initiative at Harvard University, 20 Garden Street, Cambridge, MA 02138, USA
[13] Yale Center for Astronomy & Astrophysics, Physics Department, New Haven, CT 06520-8120, USA
[14] Instituto de Astrofísica de Canarias, E-38205, C/ Vía Láctea, s/n, La Laguna, Tenerife, Spain
[15] Leiden Observatory, P.O. Box 9513, 2300 RA Leiden, The Netherlands
[16] Cahill Center for Astronomy and Astrophysics, California Institute of Technology, Pasadena, CA 91125, USA
[17] Frontier Research Institute for Interdisciplinary Sciences, Tohoku University, Sendai 980-8578, Japan
[18] Department of Physics and Astronomy, University College London, Gower Street, London WC1E 6BT, UK
[19] European Southern Observatory, Karl-Schwarzschild-Str. 2, D-85748 Garching bei München, Germany
[20] Centro de Astrobiología (CAB), CSIC–INTA, Cra. de Ajalvir Km. 4, 28850 Torrejón de Ardoz, Madrid, Spain
[21] Department of Astronomy and Joint Space-Science Institute, University of Maryland, College Park, MD 20742, USA
[22] Korea Astronomy & Space Science Institute, 776, Daedeokdae-ro, Yuseong-gu, Daejeon 34055, Republic of Korea
[23] Department of Astronomy, Kyoto University, Kitashirakawa-Oiwake-cho, Sakyo-ku, Kyoto 606-8502, Japan
[24] Institute of Particle Astrophysics and Cosmology, Stanford University, 452 Lomita Mall, Stanford, CA 94305, USA
[25] Department of Astronomy, University of Florida, 211 Bryant Space Science Center, Gainesville, FL 32611, USA
[26] National Radio Astronomy Observatory, 520 Edgemont Road, Charlottesville, VA 22903, USA
[27] Núcleo de Astronomía de la Facultad de Ingeniería, Universidad Diego Portales, Av. Ejército Libertador 441, Santiago, Chile
[28] Kavli Institute for Astronomy and Astrophysics, Peking University, Beijing 100871, People's Republic of China
[29] George Mason University, Department of Physics & Astronomy, MS 3F3, 4400 University Drive, Fairfax, VA 22030, USA
[30] Departamento de Astronomia, Universidade Federal do Rio Grande do Sul Porto Alegre, Brazil
[31] Centro de Astronomía (CITEVA), Universidad de Antofagasta, Avenida Angamos 601, Antofagasta, Chile
[32] KIPAC at SLAC, Stanford University, CA, USA
[33] Jet Propulsion Laboratory, California Institute of Technology, 4800 Oak Grove Drive, MS 169-224, Pasadena, CA 91109, USA
[34] School of Physics and Astronomy, Tel Aviv University, Tel Aviv 69978, Israel

Abstract

Virial black hole (BH) mass (M_{BH}) determination directly involves knowing the broad-line region (BLR) clouds' velocity distribution, their distance from the central supermassive BH (R_{BLR}), and the virial factor (f). Understanding whether biases arise in M_{BH} estimation with increasing obscuration is possible only by studying a large ($N > 100$) statistical sample of obscuration-unbiased (hard) X-ray-selected active galactic nuclei (AGNs) in the rest-frame near-infrared (0.8–2.5 μm) since it penetrates deeper into the BLR than the optical. We present a detailed analysis of 65 local Burst Alert Telescope (BAT) selected Seyfert galaxies observed with Magellan/FIRE. Adding these to the near-infrared BAT AGN spectroscopic survey database, we study a total of 314 unique near-infrared spectra. While the FWHMs of Hα and near-infrared broad lines (He I, Paβ, Paα) remain unbiased to either BLR extinction or X-ray obscuration, the Hα broad-line luminosity is suppressed when $N_H \gtrsim 10^{21}$ cm^{-2}, systematically underestimating M_{BH} by 0.23–0.46 dex. Near-infrared line luminosities should be preferred to Hα until $N_H < 10^{22}$ cm^{-2}, while at higher obscuration a less-biased R_{BLR} proxy should be adopted. We estimate f for

Seyfert 1 and 2 using two obscuration-unbiased $M_{\rm BH}$ measurements, i.e., the stellar velocity dispersion and a BH mass prescription based on near-infrared and X-ray, and find that the virial factors do not depend on the redshift or obscuration, but some broad lines show a mild anticorrelation with $M_{\rm BH}$. Our results show the critical impact obscuration can have on BLR characterization and the importance of the near-infrared and X-rays for a less-biased view of the BLR.

Unified Astronomy Thesaurus concepts: Active galactic nuclei (16); High energy astrophysics (739); X-ray active galactic nuclei (2035); Active galaxies (17)

Supporting material: figure sets, machine-readable tables

1. Introduction

Supermassive black holes (SMBHs, with black hole masses $M_{\rm BH} \sim 10^5$–$10^9\,M_\odot$) are ubiquitous in the local universe, lurking in the spheroid of almost all local galaxies (Kormendy & Richstone 1995). During active accretion phases, the SMBH is no longer dormant but shines as an active galactic nucleus (AGN), due to a surrounding accretion disk of matter, which releases gravitational energy as it infalls toward the central dark attractor. The ultraviolet emission from the inner accretion disk photoionizes nearby clouds located in the broad-line region (BLR). Under the hypothesis of a virialized BLR, whose dynamics are dominated by the central SMBH, the $M_{\rm BH}$ can be simply determined from the velocity $\Delta V_{\rm BLR}$ of the emitting gas clouds located at distance $R_{\rm BLR}$ in the BLR as $M_{\rm BH} = G^{-1}\Delta V_{\rm BLR}^2 R_{\rm BLR}$, with G being the gravitational constant. To model the unknown emission-weighted[36] geometry and dynamics of the BLR, the observed width $\Delta W_{\rm obs}$ (either the full-width-at-half maximum or the second moment of the line profile, i.e., the line dispersion $\sigma_{\rm line}$) of a Doppler-broadened photoionized element at distance $R_{\rm BLR}$ from the SMBH is used as a tracer of the true velocity in the BLR, and a correction factor f known as the virial factor is introduced (Onken et al. 2004):

$$M_{\rm BH} = f\,G^{-1}\Delta W_{\rm obs}^2 R_{\rm BLR} = fM_{\rm vir}\,, \qquad (1)$$

where $M_{\rm vir}$ is the so-called virial product or virial mass. Since it is in practice impossible to spatially resolve the BLR for statistically sized samples, time-resolved observations substitute for spatially resolved information to estimate the BLR radius, adopting the so-called reverberation-mapping technique (RM; Blandford & McKee 1982). This is gradually changing due to campaigns with the VLTI/GRAVITY instrument, which has opened the path to spatially resolved observations of the BLR around nearby AGN, allowing high angular resolution (<0.1 mas) spectral-spatial interferometric observations of the Paα (in 3C 273, see Gravity Collaboration et al. 2018) and Brγ (in IRAS 09149-6206, see Gravity Collaboration et al. 2020) line. However, this powerful technique remains limited to a small sample of AGN.

Extensive RM campaigns have found that the radius of the BLR is linked to the AGN luminosity, $R_{\rm BLR} \propto L_{\rm AGN}^\alpha$ (Bentz et al. 2006, 2009, 2013), where the slope α is consistent with expectations from photoionization ($\alpha \simeq 0.5$). The AGN continuum and the broad-line luminosity (see, e.g., Shen 2013) have been both used as a proxy for the BLR radius, which has

---

[36] Note that the geometry and dynamics of the BLR in so-called single-epoch mass estimates is emission-weighted, but in full reverberation-mapping studies, it is more properly responsivity-weighted.

allowed an efficient calibration for single-epoch (SE) BH mass estimation.

The virial factor f has been directly inferred only for a limited subsample (<20) of RM AGN with sufficient high-quality data available (Pancoast et al. 2014, 2018; Grier et al. 2017; Li et al. 2018; Williams et al. 2018). Hence, previous studies have often adopted an ensemble virial factor $\langle f \rangle$ that is determined using the $M_{\rm BH}$–$\sigma_\star$ relation observed in local samples of quiescent galaxies with dynamically based BH masses (Grier et al. 2013; Ho & Kim 2014; Batiste et al. 2017; Yu et al. 2019)

$$M_{{\rm BH},\sigma_\star} = \langle f \rangle M_{\rm vir}. \qquad (2)$$

However it is still unclear whether the $M_{\rm BH}$–$\sigma_\star$ relation is universally followed by all types of galaxies, e.g., barred/unbarred hosts (Graham 2008), early-/late-type hosts (McConnell & Ma 2013; Sahu et al. 2019), elliptical- and classical-/pseudo-bulges (Kormendy & Ho 2013; Saglia et al. 2016; de Nicola et al. 2019). It is also unsettled whether AGN should follow the scaling relations determined by quiescent galaxies (Woo et al. 2013; Ricci et al. 2017b; Shankar et al. 2019), since the methods used to measure the BH masses in active galaxies are not expected to suffer from the resolution-dependent bias that instead affect dynamical-based BH mass estimates (Bernardi et al. 2007; Shankar et al. 2016). Moreover, the f-factor could change on an object-by-object basis if it depends on some AGN properties, such as the bolometric luminosity, Eddington ratio ($\lambda_{\rm Edd}$), $M_{\rm BH}$, obscuration, or line-of-sight inclination angle θ. The only statistically sound correlation found so far is between f and θ, although this is based on a limited number of RM objects with directly inferred f. This correlation is consistent with expectations of the BLR being a thick disk with clouds moving in a combination of elliptical and inflowing motions (Williams et al. 2018). This f–θ relation is corroborated by statistical studies that used a variety of f-independent BH mass measurements to infer the virial factor, such as the bulge-luminosity-based BH mass (Decarli et al. 2008), the stellar-velocity-dispersion-$\sigma_\star$-based BH mass (Shen & Ho 2014), and the accretion-disk-based BH mass (Mejía-Restrepo et al. 2018). These studies only focused on optical broad-line AGN, for which optical virial-based $M_{\rm BH}$ estimates were available.

While the use of the Hα emission is common practice to derive $M_{\rm BH}$ in statistical samples to study the demography and evolution of the AGN population, it is unclear whether the Hα is completely reliable, particularly in so-called Sy 1.9 (Osterbrock 1981), where the level of extinction due to dust is more relevant than what is usually experienced in optical broad-line Seyferts. Indeed Reines & Volonteri (2015), using a sample of 262 broad-line AGN in the nearby universe ($z < 0.055$) with Hα broad lines measured from the Sloan Digital Sky Survey (SDSS) DR8, find that AGN-hosts with SE

Hα-based BH masses define a separate M_{BH}–$M_\star$ relation, with a slope similar to that of early-type galaxies with dynamically detected BHs but with a normalization $\sim$1.2 dex lower. Similarly, Koss et al. (2017) show that the SE Hα-based BH masses in Sy 1.9 are undermassive than what is expected from the M_{BH}–$\sigma_\star$ relation of elliptical-/classical-bulges, with the BH mass deviation being more extreme in sources with broad Hα equivalent width EW < 50 Å. Additionally, Caglar et al. (2020) find an offset of $\sim$0.6 dex between the SE Hα-based BH masses and those based on the stellar velocity dispersion in a sample of 19 partially obscured local hard X-ray-selected Seyferts from the LLAMA sample. This discrepancy is reduced in the LLAMA sample only after accounting for optical extinction, in the Hα measurement, and galaxy rotation, in the $\sigma_\star$ estimate (Caglar et al. 2020). These results can be explained either with the fact that BH-host scaling relations should be different in active versus inactive galaxies or with the fact that in some cases the Hα-based BH masses could be biased low in the presence of extinction (or with a combination of these two effects).

To this end, the rest-frame near-infrared (NIR, 0.8–2.5 μm) band allows for a deeper probe of the physical condition of the BLR gas, being at least a factor of 10 less affected by dust extinction than the rest-frame optical emission (Goodrich et al. 1994; Veilleux et al. 1997; Veilleux 2002). However, NIR ground-based spectroscopic observations are more complex and time-consuming than optical spectroscopy, due to the lower atmospheric transmission that reduces the observable windows, bright sky background, and strong-OH sky line emissions. For these reasons, local AGN samples studied so far have remained limited to few objects, usually $\lesssim$50 (Glikman et al. 2006; Riffel et al. 2006, 2015; Landt et al. 2008; Mason et al. 2015; Onori et al. 2017a).

Determining the BLR properties and *f*-factors for a less-biased AGN sample is of paramount importance to assess the uncertainties and systematics in M_{BH} measurement in active galaxies as a function of obscuration. This is particularly important for Sy 1.9s, where the only optical broad line available is the Hα, and Sy 2s, where sometimes so-called hidden BLR are found in the NIR ($\sim$30% of cases, see, e.g., Veilleux et al. 1997; Riffel et al. 2006; Cai et al. 2010; Smith et al. 2014; Lamperti et al. 2017; Onori et al. 2017a). Such an investigation is only possible by constructing an obscuration-unbiased AGN sample, by means of hard X-ray (>10 keV) AGN selection that is almost unaffected by intervening obscuring material, at least up to $N_H \sim 10^{23.5}$–10^{24} cm^{-2} (Ricci et al. 2015; Koss et al. 2016), due to the decline of the photoelectric cross section with increasing photon energy. A sensitive all-sky survey in the ultrahard X-ray band (14–195 keV), such as the one carried out by the Burst Alert Telescope (BAT; Barthelmy 2000) on the Neil Gehrels Swift Observatory (Swift/BAT), coupled with NIR spectroscopy and ancillary optical spectroscopic information, is the ideal database to quantify the effects of obscuration on BLR characterization and thus BH mass estimation. The BAT AGN Spectroscopic Survey (BASS)[37] has for the first time increased the sample size of AGN surveyed with NIR spectroscopy to more than 100 beginning with the DR1 (Lamperti et al. 2017).

In this work, we present NIR Magellan spectra of 65 local Seyferts, selected from the 70 months Swift/BAT catalog (Baumgartner et al. 2013), as part of the BASS survey. We complement our NIR Magellan sample with the NIR BASS database, NIR DR1 (Lamperti et al. 2017), DR2 (den Brok et al. 2022),[38] to construct the largest sample of local Seyferts with NIR and X-ray spectral information available to date, for a total of 314 unique NIR spectra. We further complement the NIR analysis with optical spectral information on the broad component of the Hα from the optical BASS DR2 (Mejía-Restrepo et al. 2022), to quantify and compare the BLR characterization in both optical and NIR. We finally make use of the optical stellar velocity dispersion measurements available in BASS DR2 (T. Caglar et al. 2022, in preparation) to infer the individual *f* factors of our sample.

The work is organized as follows: Section 2 presents the Magellan data selection and reduction; Section 3 describes the Magellan spectral fitting of the most important NIR emission lines; Section 4 is devoted to the descriptions of two independent BH mass measurement methods adopted to derive the virial factors *f*. Results are described in Section 5, where we investigate the fraction of hidden BLRs detected in Sy 1.8–1.9–2 (Section 5.1), the effects of X-ray obscuration and BLR extinction on the BLR velocity and radius tracers derived from optical (i.e., Hα) and NIR emission lines (He Iλ10830, Paβ λ12821, Paα λ18756) in Sy 1–1.9 (Section 5.2) and in Sy 1–2 (Section 5.4). In Section 5.3, we explore the connection between the material responsible for BLR extinction and the one absorbing the X-rays. The virial factors of our sample are derived in Section 5.5, where we test whether *f* depends on some parameters, e.g., *z*, N_H and BH mass. Section 6 is devoted to discussions and conclusions, while Section 7 briefly summarizes our main results. We adopt the concordance cosmological model, $\Omega_M = 0.3$, $\Omega_\Lambda = 0.7$, and $h = 0.7$.

2. Data

Here we present the NIR spectroscopic data (PI: E. Treister, F. Ricci, M. Baloković)[39] obtained at Magellan using the Folded-port InfraRed Echellette (FIRE; Simcoe et al. 2008). The Magellan/FIRE sample was selected from the hard X-ray (14–195 keV) 70 months catalog (Baumgartner et al. 2013) without NIR coverage in the BASS DR1 (Lamperti et al. 2017), as part of an effort within the BASS collaboration to obtain NIR coverage for an obscuration-unbiased census of local accreting SMBHs. The 70 month catalog (Baumgartner et al. 2013) listed 838 AGN, 102/838 were targeted in the BASS DR1 (Lamperti et al. 2017), and 118/838 were observed as part of the DR2 (den Brok et al. 2022), which selected as well an additional 50/1016 AGN from the latest 105 months source catalog (Oh et al. 2018). The combined sample totals 314 hard X-ray-selected AGN with unique NIR spectra. The FIRE sample was chosen to target the more obscured sources, to estimate the M_{BH} also in obscured Seyfert class AGN (i.e., Sy 1.8–1.9–2). The FIRE sample is composed of 65 targets selected at $z \lesssim 0.2$, divided into 52 obscured AGN (i.e., Sy 1.8–1.9–2) and 13 optical broad-line AGN (i.e., Sy 1–1.2–1.5), whose Seyfert classification is defined according to the Osterbrock (1981) standard criteria, using optical spectra collected by BASS (e.g., BASS optical DR2; Mejía-Restrepo

---
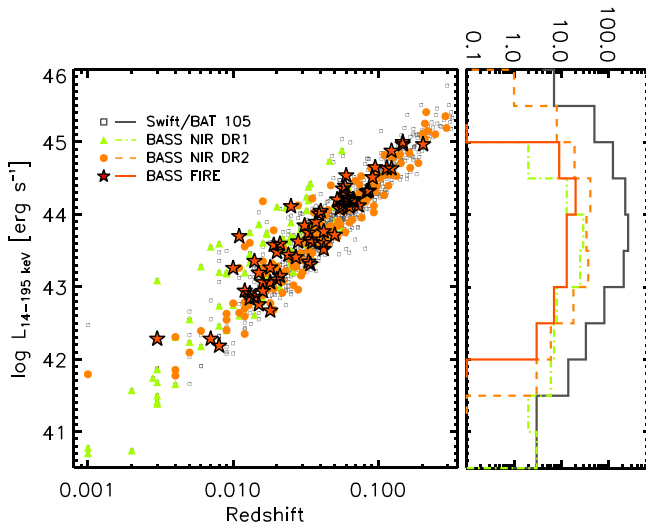
Figure 1. Left: the $L_{14-195\,\mathrm{keV}}$–z distribution of the FIRE sample, BASS NIR DR1 (Lamperti et al. 2017), BASS NIR DR2 (den Brok et al. 2022), and BAT 105 months sample (Oh et al. 2018). Colors and symbols according to the legend. Right: histogram of the hard X-ray luminosities.

et al. 2022). Figure 1 shows the $L_{14-195\,\mathrm{keV}}$–z distribution of the FIRE targets (red stars), BASS NIR DR1 (green triangles; Lamperti et al. 2017), BASS NIR DR2 (orange filled circles; den Brok et al. 2022), and the latest 105 months Swift/BAT catalog (dark-gray open squares; Oh et al. 2018).

The FIRE data is complementary to the BASS NIR DR1 and DR2, spanning ∼3 dex of overlap in X-ray luminosity (see, right panel in Figure 1), and aside from some lower L_X and lower-z object of the DR1 and some higher-L_X and higher-redshift source in the DR2, all three BASS samples should be studying AGN with similar properties. The combined NIR data set is representative of the parent BAT AGN sample.

The 65 NIR 0.8–2.5 μm spectra were observed using the FIRE instrument in the high-resolution echelle mode in four visiting runs carried out between 2018 April and 2019 April. FIRE is a dual-mode IR spectrometer mounted at the Magellan Baade telescope at Las Campanas Observatory (LCO), Chile. Its primary mode employs a combination of a diffraction grating and four prisms to deliver cross-dispersed spectra covering the whole NIR bandpass in a single exposure, with nominal wavelength resolution of $R = \lambda/\Delta\lambda \approx 6000$ for a $0''.6$ slit width, i.e., $\Delta v \simeq 50$ km s^{-1}. This slit width was adopted for our program, with the exception of two targets, namely BAT 677 and 1085, which were observed with a $0''.45$ slit width (i.e., $R \approx 8000$, $\Delta v \simeq 37$ km s^{-1}), since those were expected to have low M_{BH}. Our observations took place the nights of UT 2018 April 5, UT 2018 September 30, UT 2019 March 9, and UT 2019 April 14–15 during gray time. The observations were executed under clear skies with different airmass conditions (see Table 1) and visual seeing varying between $1''.5$ and $0''.4$, with an average of $0''.75$.

For each target, the individual spectra were obtained using the nodding technique in a sequence of ABBA acquisitions, with exposure times ranging between 190 and 623 s (multiples of 10.6 s, since sample-up-the-ramp SUTR readout mode was used for all targets but the ones marked with an asterisk in Table 1, which were observed using Fowler 4 readout), depending on target magnitude and observing conditions. The acquisition sequence involved a short arc frame (ThAr) just after the target observation in order to correct for telescope

flexure and obtain the wavelength solution. For long (>300 s) exposures, OH airglow was used to improve the wavelength calibration. By default, the wavelengths are calibrated in vacuum. Sky and dome (Qz) flats were acquired to correct for detector illumination and pixel gain variations across the slit, respectively. Data were reduced with the IDL pipeline `FireHose` v2 package (Gagné et al. 2015), which performs 2D sky subtraction and extracts an optimally weighted 1D spectrum. Nearby A0V stars were observed during the night in order to derive relative flux calibrations. We corrected the atmospheric absorption features (H_2O, CO_2, CH_4, and O_2) using the software tool `molecfit` (Smette et al. 2015). `Molecfit` uses a radiative transfer code to simulate the atmospheric transmission, taking into account local weather parameters (temperature, pressure, humidity, etc.), recorded at the LCO/Magellan site.

Flux-calibrated and redshift-corrected NIR spectra of the 65 AGN are shown in Figure 2 (as a figure set) smoothed using a Savitzky–Golay filter, which preserves the average resolving power. The spectra are ordered by their BAT ID in Figure 2. Regions of low telluric transmission are plotted in gray. The locations of some of the most intense NIR emission lines are labeled and indicated with dashed purple lines in Figure 2. The reduced spectra will be available on the BASS survey website.[40]

3. Spectral Measurements

Below we describe the NIR emission-line fitting analysis of the FIRE spectra.

3.1. Near-infrared Spectral Fitting Procedure

Our emission-line fitting approach is similar to the one adopted for the BASS NIR DR1 (e.g., Lamperti et al. 2017) and DR2 (den Brok et al. 2022). We use `PySpecKit` (v0.1.21), an extensive spectroscopic analysis toolkit for astronomy, which uses a Levenberg–Marquardt algorithm (Ginsburg & Mirocha 2011). We fit the Paζ (0.9−0.96 μm), Paγ (1.04−1.15 μm), Paβ (1.15−1.30 μm), and Paα (1.80−2.00 μm) spectral regions separately, to ease the fitting convergence. Each so-defined independent spectral region contains at maximum three lines coming from permitted species in the BLR. There are only a few differences with the emission lines considered in Lamperti et al. (2017, see their Table A1), which are the following: we fit also the [N I]$\lambda10404$ in the Paγ region and the Brϵ $\lambda18179.1$, H II$\lambda18345$, He I$\lambda18635$, and [S XI]$\lambda19196$ in the Paα region, while we did not include in the fit [Fe II]$\lambda9227$ in the Paζ spectral region, since it is a faint iron emission and was not detected in our FIRE observations.

We first deredden the spectra using the Galactic extinction value $E(B-V)$ (Schlafly & Finkbeiner 2011) as listed in the IRSA Dust Extinction Service,[41] and redshift correct the spectra. We employ a single first-order power-law fit to model and remove the continuum. For each spectral region, we estimate the continuum level using sections of the wavelength range free of emission lines, i.e., excluding 20 Å around the narrow lines and 150 Å where a broad component was expected, e.g., in permitted species.

---

[40] https://www.bass-survey.com/
[41] https://irsa.ipac.caltech.edu/applications/DUST/

Table 1
Magellan/FIRE Observation Log

BAT ID	Counterpart Name	Class	Obs. Date dd.mm.yy	Exposure (s)	Airmass	J (mag)	z	Slit/Aperture		$\log L_{2-10\,\mathrm{intr}}$ (erg s^{-1})
								($''$)	(kpc)	
(1)	(2)	(3)	(4)	(5)	(6)	(7)	(8)	(9)	(10)	(11)
7	SDSSJ000911.57-003654.7	Sy2	30.09.18	4 × 306	1.14	14.74	0.073	0.6/0.74	0.93/1.15	43.60
10	LEDA1348	Sy1.9	30.09.18	4 × 370	1.02	14.67	0.095	0.6/0.68	1.28/1.44	44.40
80	2MASXJ01290761-6038423	Sy2	30.09.18	4 × 370	1.17	15.17	0.203	0.6/0.82	4.23/5.80	45.23
118	3C62	Sy2	30.09.18	4 × 370	1.04	15.43	0.147	0.6/0.69	2.39/2.74	44.50
238	LEDA745026	Sy2	05.04.18	8 × 190	1.33	15.44	0.147	0.6/0.34	2.41/1.36	44.42
262	ESO553-22	Sy2	30.09.18	4 × 190	1.13	13.89	0.042	0.6/0.76	0.52/0.66	43.38
272	IRAS05189-2524	Sy2	30.09.18	4 × 190	1.07	13.11	0.042	0.6/0.54	0.52/0.46	43.40
305	LEDA17883	Sy2	30.09.18	4 × 190	1.28	14.63	0.050	0.6/0.86	0.62/0.89	43.51
329	ESO121-28	Sy1.9	05.04.18	8 × 190	1.29	13.89	0.040	0.6/1.00	0.50/0.83	43.63
372	1RXSJ072720.8-240629	Sy1.9	30.09.18	4 × 370	1.33	15.06	0.123	0.6/0.52	1.83/1.59	44.34

Note. Columns are as follows: (1) 70 months Swift/BAT ID (https://swift.gsfc.nasa.gov/results/bs70mon/); (2) associated counterpart name; (3) optical Seyfert classification, as defined by Osterbrock (1981); (4) observation date; (5) exposure time; (6) airmass at the midpoint of the observation; (7) J-band Vega mag (from 2MASS extended, e.g., Jarrett et al. 2000); (8) redshift from the [O III] BASS DR2; (9)–(10) slit width and aperture of the spectral extraction, in arcseconds and kiloparsecs; (11) intrinsic 2–10~keV luminosity from Ricci et al. (2017a).

(This table is available in its entirety in machine-readable form.)

As the focus of our investigation is to study the BLR properties, the main goal is to derive the FWHM and flux of broad-line species. Emission lines are modeled using a combination of Gaussian profiles, namely one component for all line species associated with the NLR and an additional Gaussian to account for the BLR component in all permitted transitions of each spectral region. The relative central wavelengths of the narrow lines are tied together, but are allowed to shift together by a maximum of 500 km s^{-1} with respect to the systemic redshift listed in Table 1. As an initial input value for the width of the narrow lines, we used the best-fit width of the [S III]λ9531 line, which is the strongest (and the narrowest, see, e.g., Figure 3 in Riffel et al. 2013) narrow emission line in the rest-frame NIR wavelength range, with only a minor blending with the Paϵ on its red side. The widths of the narrow components in each spectral region are then tied together.

The threshold between narrow and broad components is set at FWHM = 1200 km s^{-1}, as consistent with the division defined in BASS NIR DR1 (Lamperti et al. 2017). The central wavelengths of the broad components are allowed to shift up to $\approx$1000 km s^{-1} (Shen et al. 2016). Since the widths of the broad components in each spectral region are likely to be similar, we tie them together to avoid unnecessary complexity and degeneracy.[42] As each spectral region is fitted separately, the resulting best-fitting BLR component can be different in each region. The same applies to the NLR estimate, which might vary in different spectral regions. The fit is thus run a first time. Lines are detected if their amplitude is >3σ, where σ is the root mean square of a line-free zone in each spectral region. After the first minimization, (1) if the strongest narrow transition of each region is not detected, we fixed the width of the narrow component to the [S III]λ9531, and (2) if the broad component of a line is below the detection threshold, we discard the component as an unreliable detection, and we run again the fit,

using only a single narrow Gaussian component. In a few cases, after visual inspection, additional Gaussian components were added to the model in order to improve the fit. These additional velocity components do not contribute to the broad component used to compute the BH mass (Section 4) as they are not considered as BLR tracers.[43] In particular, in the Paγ region, 7/65 spectra required one additional intermediate velocity component in the He Iλ10830, (i.e., BAT IDs 372, 488, 577, 698, 744, 1064, and 1079); in the Paα region, 1/65 required an additional intermediate velocity component in the Paα (BAT 1079), and 1/65 required one additional intermediate velocity component in the Paα and two additional lines H IIλ18345 and H IIλ189205 (BAT 372). The model with additional Gaussians was run twice as in the normal case, in order to discard the components in case those were below the detection threshold. We then correct the measured FWHMs to account for instrumental resolution, even though it is not a substantial correction for broad lines.

To estimate the uncertainties related to emission-line measurements in each spectral region, we repeated the fit ten times, adding each time an amount of noise σ randomly drawn from a normal distribution with the deviation equal to the noise level. We computed the median absolute deviation of the ten measurements, and we used this value as an estimate of the uncertainty at the 1σ confidence level (c.l.). We estimate the flux upper limits (at 3σ) on the (undetected) broad-line components by assuming a FWHM = 4200 km s^{-1}, which is the average FWHM of the broad-line detections in our FIRE data set. We then visually inspected all the fits and assigned quality flags, following the classification nomenclature of the first BASS paper (Koss et al. 2017). Quality flag 1 refers to spectra that have small residuals and very good fits. Flag 2 means that the fits are not perfect, but still acceptable. Flag 3 is assigned to not completely satisfactory fits for high signal-to-noise ratio (S/N) sources due to the presence of either absorption lines, additional components in the fit, or structure in the residuals, making the fit decomposition more uncertain.

---

[42] We checked that the best-fit NIR broad lines in separate regions, which have been fitted independently, thus without imposing any common constraint on their widths, are consistent within the uncertainties, as also previously reported in the literature (see Landt et al. 2008; Lamperti et al. 2017; Onori et al. 2017a; Ricci et al. 2017c).

[43] We note that, even considering the additional component as coming from the BLR, our results do not change since those (few) cases do not fulfill one or more of the criteria we adopt in the subsequent analysis.
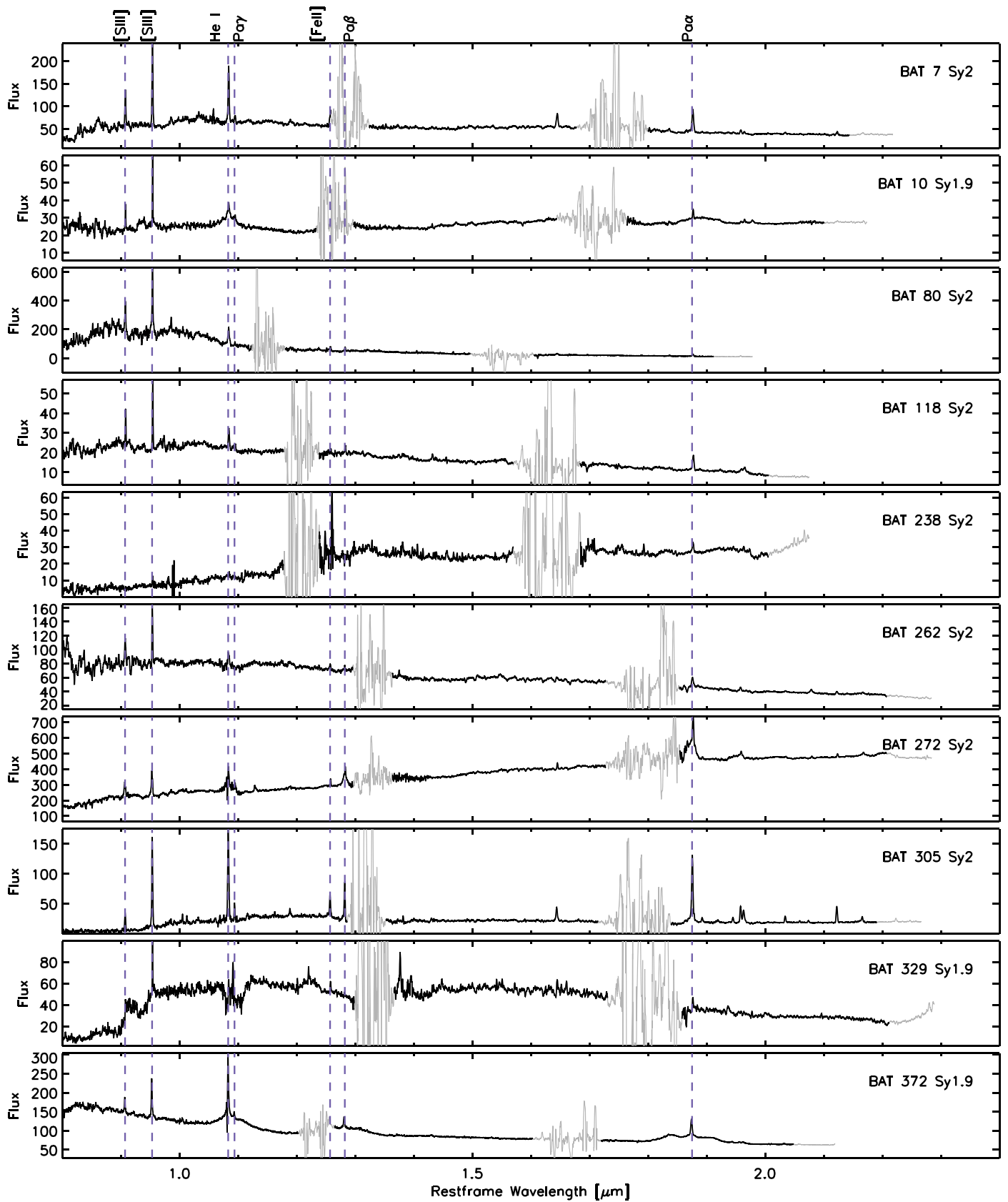
Figure 2. Examples of FIRE/Magellan NIR spectra in units of $\times 10^{-17}$ erg s^{-1} cm^{-2} Å^{-1}, redshift-corrected and flux calibrated. The wavelength position of some of the most relevant emission lines are indicated with dashed vertical lines and labeled at the top. Regions of low telluric transmission are shown in gray. The complete figure set for the 65 AGN is available online, ordered by BAT ID.

(The complete figure set (7 images) is available.)
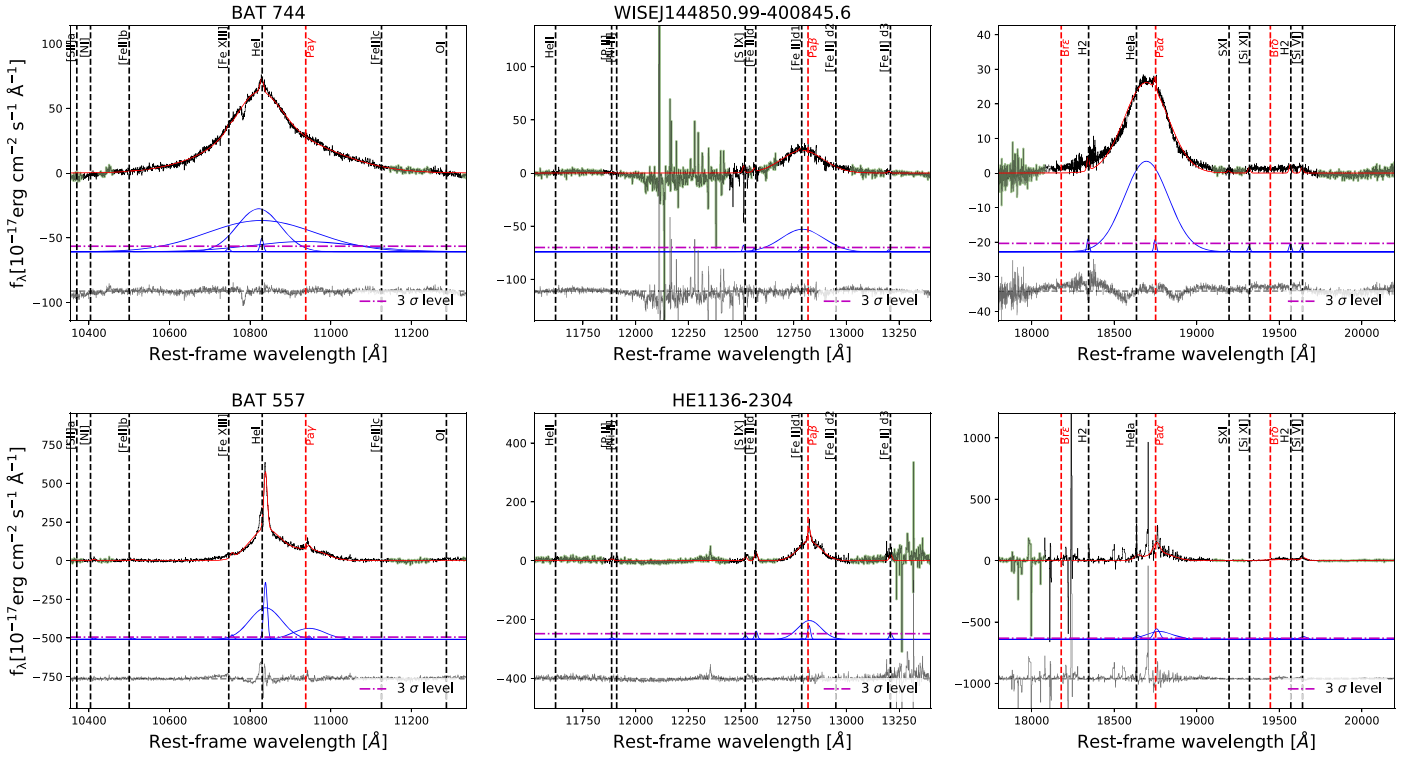
Figure 3. Examples of spectral emission-line fits of the Paγ (left), Paβ (center), and Paα (right) regions for a Sy 1 (BAT 744, top) and a Sy 1.9 (BAT 557, bottom). The best-fit Gaussians are plotted in blue. As explained in Section 3.1, a broad Gaussian component is discarded if its intensity is below 3σ (dashed purple line) with respect to the fitting continuum. The continuum has been evaluated in the regions highlighted in green and subtracted off. In red the resulting total model is shown. Residuals are plotted offset in dark gray. The fit quality flags are as follows: 2, 2, and 1 in the Paγ, Paβ, and Paα regions of BAT 744, respectively; and 2, 1, and 4 in the Paγ, Paβ, and Paα regions of BAT 557, respectively. The complete figure set with all the 65 FIRE/Magellan spectral emission-line fits in the Paγ, Paβ, and Paα regions is available online.

(The complete figure set (13 images) is available.)

Flag 4 refers to spectra with low S/N and/or strongly affected by telluric residuals; the best-fit NLR and BLR estimates are highly uncertain. Flag 9 refers to spectra where no emission line is detected. The results of the broad emission-line fits are presented in Tables A1–A3 for the Paγ, Paβ, and Paα broad lines. Tables A4–A5 report the few cases that needed additional components in their spectral fit. Figure 3 shows examples of emission-line fits for a Sy 1, BAT 744 (top panels), with fit quality flags 2 (2,1) in the Paγ (Paβ, Paα) regions, and for a Sy 1.9, BAT 557 (bottom panels), with fit quality flags 2 (1,4) in the Paγ (Paβ, Paα) regions. The remainder of the best-fit models derived for the full FIRE data set in the spectral regions Paγ, Paβ, and Paα are shown as a figure set in Figure 3 (available online) ordered by increasing BAT number.

4. M_{BH} Measurements

Below we briefly describe the two independent M_{BH} estimates adopted in order to understand if the NIR view of the BLR gives consistent BH mass estimates compared to the more often adopted Hα-based BH mass estimate, in the case of Sy 1 up to Sy 1.9 AGN, and the $σ_⋆$-based BH mass estimates, which include Sy 2 AGN lacking broad Hα line and strong AGN continua but with NIR broad lines. Combining Equations (1)–(2), we evaluate the individual virial factors f of our sample as follows:

$$f = \frac{M_{BH,σ_⋆}}{M_{vir,line}}, \qquad (3)$$

where $M_{BH,σ_⋆}$ is the BH mass estimated from the optical stellar velocity dispersion (Section 4.1), and $M_{vir,line}$ is the virial-based BH mass estimated for each NIR broad line considered in our study (see Section 4.2).

4.1. BH Mass Estimate from the M_{BH}–$σ_⋆$ Scaling Relation

The relation between M_{BH} and the bulge stellar velocity dispersion is probably the most fundamental and most used BH-host scaling relation due to its intrinsic small scatter (∼0.3 dex Kormendy & Ho 2013; Saglia et al. 2016; Shankar et al. 2016; van den Bosch 2016; de Nicola et al. 2019; Marsden et al. 2020), and lack of strong redshift evolution, at least until $z \sim 1$ (e.g., Shen et al. 2015; Sexton et al. 2019). There are several M_{BH}–$σ_⋆$ calibrations available in the literature, some of which take into account the host morphology (late/early type, McConnell & Ma 2013; Sahu et al. 2019; barred/unbarred, Graham 2008; elliptical- and classical-/pseudo-bulges, Kormendy & Ho 2013; Saglia et al. 2016; de Nicola et al. 2019). We adopt the M_{BH}–$σ_⋆$ relation proposed by Kormendy & Ho (2013), which is calibrated on dynamical-based M_{BH} measurements of local ellipticals and classical-bulges, and for which an average virial factor $\langle f \rangle$ has already been estimated (Ho & Kim 2014; Yu et al. 2019). More recent estimates of the average virial factor determined by Batiste et al. (2017) and Yu et al. (2019) are consistent, within their (large) uncertainties, with the values found by Grier et al. (2013) and Ho & Kim (2014).

The M_{BH}–$\sigma_\star$ relation of elliptical- and classical-bulges from Kormendy & Ho (2013) is among the highest relations in normalization in the M_{BH} versus $\sigma_\star$ plane up to date (see, e.g., Figure 2 in Ricci et al. 2017b). This means that at a given velocity dispersion it predicts the largest SMBH masses, at least until predicted $M_{BH} \approx 10^9 M_\odot$. In other words, the f-factors derived using Equation (3) are the largest that can be possibly predicted with the currently calibrated M_{BH}–$\sigma_\star$ relations, even considering the most recent updates (Saglia et al. 2016; de Nicola et al. 2019). We will discuss later how this assumption affects the virial factors f and our analysis.

4.2. BH Mass Estimate from the Virial Method

The virial M_{BH} estimate implicitly assumes that the motion of clouds in the BLR is virialized. Thanks to the R–L relation established by RM campaigns (see, e.g., Bentz et al. 2013), Equation (1) can be rewritten using easily accessible quantities, like broad emission line or continuum luminosity. We adopted the mixed virial BH mass estimator put forward by Ricci et al. (2017c), for a similar mixed M_{BH} virial estimator; see also Bongiorno et al. (2014), La Franca et al. (2015). The virial BH mass estimator proposed by Ricci et al. (2017c) is based on either optical (e.g., Hβ or Hα) or NIR (Paα, Paβ, or He Iλ10830[44]) FWHM and on hard X-ray luminosities, either 2–10 or 14–195 keV. Thus, we can compute the virial BH mass $M_{vir,line}$ using the 14–195 keV luminosity L_X and any single broad line reliably detected, i.e., He I, Paβ, and Paα. The use of the observed BAT luminosity does not affect our analysis since the majority of our sample has $N_H < 10^{23.5}$ cm^{-2}, and the observed 14–195 keV luminosity is almost unaffected by X-ray absorbing columns up to at least $N_H \sim 10^{23.5}$–10^{24} cm^{-2} (Ricci et al. 2015; Koss et al. 2016).

We can also compute the mass with the FWHM of all the reliable detections and with the weighted[45] average, in the presence of more than one reliable detection. We call this case NIR[46] in all subsequent analyses. The mixed virial mass is thus $M_{vir,line} \propto$ FWHM(line)$^2 \times L_X^{0.5}$, with $line$ being He I, Paβ, Paα, and NIR samples. The statistical uncertainties on the virial BH mass estimate are then the combination of the errors on the broad FWHM and on the X-ray luminosity $L_{14-195\,keV}$. For simplicity, we assumed a 5% uncertainty on the hard X-ray luminosity; while for the FWHM, we used the uncertainties determined from the spectral fit. The aforementioned statistical uncertainty does not take into account the intrinsic spread of virial BH mass estimates, which is of the order of $\sim$0.5 dex (McLure & Jarvis 2002; Vestergaard & Peterson 2006; Ricci et al. 2017c).

As for the majority of the virial BH mass estimators, the relations in Ricci et al. (2017c) were calibrated against a sample of local RM AGN with Hβ measurements, and therefore an average virial factor $\langle f \rangle$ was adopted. This $\langle f \rangle$ changes depending on whether the RM calibrating virial masses are based on the FWHM or the second moment of the line profile

σ_{line} (see, e.g., Onken et al. 2004; Collin et al. 2006) such that

$$f_\sigma = f_{FWHM} \times \left(\frac{FWHM}{\sigma_{line}} \right)^2. \qquad (4)$$

The relations calibrated by Ricci et al. (2017c) adopt as a calibration sample the RM virial masses based on the Hβ line dispersion measured from the rms spectra, $\sigma_{H\beta,rms}$ (Ho & Kim 2014), and in particular the value $\langle f_\sigma \rangle = 4.31 \pm 1.05$, derived in Grier et al. (2013) by requiring that RM AGN reproduce the M_{BH}–$\sigma_\star$ relation found in quiescent galaxies by Woo et al. (2013). Alternatively, Ricci et al. (2017c) also calibrated BH mass estimators considering the bulge morphology, proposing BH mass estimators also for classical-bulges, $\langle f_\sigma \rangle = 6.3 \pm 1.5$, and pseudo-bulges, $\langle f_\sigma \rangle = 3.2 \pm 0.7$. These $\langle f_\sigma \rangle$ values were determined in Ho & Kim (2014) to put RM AGN virial BH masses on the M_{BH}–$\sigma_\star$ relation of classical-bulges, given by Kormendy & Ho (2013), and the one followed by pseudo-bulges, determined by Ho & Kim (2014). For more details on the BH mass estimators, see Table 4 in Ricci et al. (2017c).

Since the chosen reference BH–$\sigma_\star$ relation is the one from Kormendy & Ho (2013; see Section 4.1), we adopt the BH mass relation based on the $\langle f_\sigma \rangle = 6.3$, which is relation b3 in Table 4 of Ricci et al. (2017c), in the classical-bulge case

$$\left(\frac{M_{BH}}{M_\odot} \right) = 10^a \cdot \left[\left(\frac{FWHM}{10^4\ km\ s^{-1}} \right)^2 + \left(\frac{L_X}{10^{42}\ erg\ s^{-1}} \right)^{0.5} \right], \quad (5)$$

with $a = (7.96 \pm 0.02)$.

In order to more easily compare with literature works about the f-factor (see, e.g., Collin et al. 2006; Decarli et al. 2008; Shen & Ho 2014; Mejía-Restrepo et al. 2018), we convert the individual f-factors from f_σ to f_{FWHM} using Equation (4) and assuming the FWHM/σ_{line} ratio for a single Gaussian case, i.e., $\sqrt{8 \ln 2} \approx 2.355$. This is equivalent to rescale the $\langle f_\sigma \rangle$ adopted as $6.3/(2.355)^2$. We denote this rescaled average virial factor as f_0. The symbol f_0 is hence the equivalent to writing $\langle f_{FWHM} \rangle$, and it is the average value adopted to convert the virial BH mass $M_{vir,line}$ to the BH mass $M(line)$, i.e., $M(line) = f_0 \times M_{vir,line}$. With this notation, the f derived in Section 5.5 using Equation (3) will be, strictly speaking, a f_{FWHM}. From now on, we will drop the suffix FWHM and simply write f when referring to f_{FWHM}.

When optical broad Hα mass estimates are available from the BASS DR2 (Mejía-Restrepo et al. 2022), we compare them to the NIR-based virial BH mass estimated here (see, Section 5.2). These optical BH masses are computed with the prescription proposed by Greene & Ho (2005, see, e.g., their Equation (6)), based on the FWHM and luminosity of the broad Hα, with virial factor of unity (Mejía-Restrepo et al. 2022).

5. Results

To help the reader, we here present a brief summary of the topics in the results section. In Section 5.1, we introduce the sample of Sy 1.8–1.9–2 types for which we reliably detect NIR broad lines. We compare in Section 5.2 the NIR and optical, i.e., Hα, broad-line widths to understand if the ability of measuring the BLR velocity and radius changes with increasing obscuration/extinction. We then examine how the medium responsible for obscuring the BLR is related to the material

---

[44] From now onward, He Iλ10830 is called just He I.
[45] The weights are the square of the inverse of the measured broad-line FWHM uncertainties, $1/\sigma_i^2$
[46] The term NIR in *italic* should not be confused with the general term NIR that indicate the 0.8–2.4 μm wavelength range.
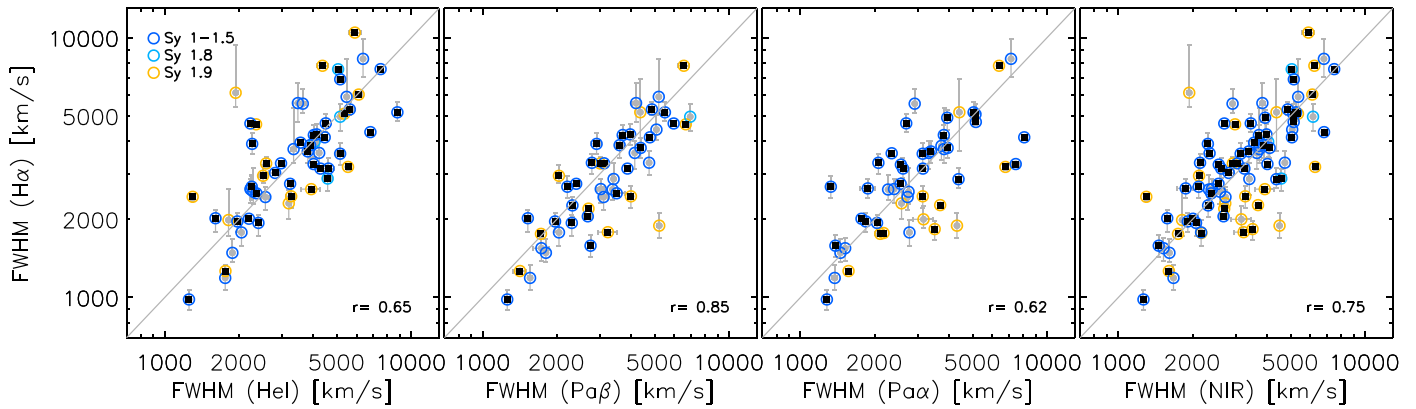
Figure 4. Hα vs. NIR BLR velocities for BASS targets, from left to right: He I, Paβ, Paα, and *NIR* broad-lines samples, respectively. The *NIR* sample is the collection of reliably detected NIR broad-line FWHM, being the weighted average FWHM in case there is more than one reliable broad-line detection. The colored circles mark the Sy 1–1.5 (blue), Sy 1.8 (cyan), and Sy 1.9 (orange) types. Only targets with reliable Hα and NIR detection in each line, as defined in Sections 5.1 and 5.2.1, are shown. The black filled squares are the more robust optical measurements, having <10% uncertainties in the broad FWHM (Hα). Pearson correlations coefficients *r* computed for the more robust subsample (black squares), without separating between Sy subclasses, are reported in each panel.

absorbing the X-rays in Section 5.3. By investigating the effect of X-ray obscuration on Hα and NIR broad-line luminosities, we demonstrate that the use of Hα (Section 5.2.2) and NIR (Section 5.4) broad-line luminosities in SE BH mass determinations induce a bias in the BH mass measurements when the column density is above a certain threshold. Finally in Section 5.5, we compare two independent obscuration-unbiased BH mass measurements, derive the virial factors, and examine whether they depend on some additional parameters.

5.1. Broad-line Detection in Reddened Seyferts

This work is composed of 33 Sy 2, 18 Sy 1.9, and 1 Sy 1.8, or a total of 52 reddened Sy types. As stated in the introduction, in ∼30% of cases, Sy 1.8 to 2 with narrow emission lines in the rest-frame optical spectra have been found to exhibit broad hydrogen and helium recombination lines, i.e., Paα, Paβ, and He I. We focus mainly on these three emission lines since all higher-order Paschen transitions are strongly blended with emission lines from other elements, and He I, even though blended with Paγ, is among the most intense rest-frame NIR lines (see, e.g., Figure 9 in Riffel et al. 2006), and therefore it is possible to detect and deblend faint broad components relatively easily. The rest-frame NIR also contains the hydrogen Brackett series, the strongest emission being the Brγ λ21661. The Brγ is isolated, located in a region less affected by low atmospheric transmission, and redder than Paα; thus effects of dust extinction are expected to be even lower. However, its intensity is rather low compared to the Paschen and helium lines (Brγ/Pa $\beta \approx 0.16$ in case B with $T = 10^4$ K and density $n = 10^6$ cm^{-3}; see, e.g., Osterbrock & Ferland 2006), thus we do not investigate its properties in this work. Based on the fact that the He I, Paβ, and Paα lines have been found to have similar FWHMs in Sy 1 and in intermediate types (Landt et al. 2008; Lamperti et al. 2017; Onori et al. 2017a; Ricci et al. 2017c; see also Section 5.2 and in particular Figure 4), we can also examine the collection of NIR broad-line measurements, which we call *NIR*. When more than one observation was present, we chose the one with the highest S/N evaluated on the continuum, in each spectral region. Combining the DR1, DR2, and FIRE observations, the total parent sample is thus composed of 235 obscured BASS AGN, divided into 168 Sy2, 60 Sy 1.9, and 7 Sy 1.8.

Considering only the most reliable measurements, i.e., only the cases where the spectral fit quality is good (quality flag equal to 1 or 2) and the relative uncertainty on the measured broad FWHM is < 10%, the final reliably detected broad lines are 63/235 (27^{+4}_{-3}%) combining the number of detections of at least one of the above transitions. The broad-line detection rate is expected to be consistent in the three BASS samples since the targeted AGN should be similar in their properties (see Figure 1).[47]

5.2. Optical and Near-infrared View of the BLR in Sy 1–1.9

It is important to understand whether the measured-Hα broad-line width and luminosity are accurately tracing the underlying BLR motion and radius, particularly for intermediate Sy 1.8 and 1.9 where the extinction is higher than in the normal optical broad-line AGN. The NIR offers a view of the BLR complementary to the optical, as it can help penetrate into the innermost and fastest-moving BLR clouds. Together with X-ray ancillary data provided by BASS (Ricci et al. 2017a), NIR spectroscopy can help to understand biases or systematics in BLR measurements, e.g., the BLR velocity and radius, obtained from the Hα (BASS DR2; Mejía-Restrepo et al. 2022).

Indeed, a large community effort is being spent to find intermediate mass BHs ($M_{\rm BH} < 10^5 M_\odot$, Greene & Ho 2004, 2007; Reines et al. 2013; Moran et al. 2014; Baldassare et al. 2017; Mezcua 2017; Chilingarian et al. 2018; Mezcua et al. 2018; Martínez-Palomera et al. 2020), as this population has a huge impact on several aspects concerning BH seed formation and BH growth at high redshift (see, e.g., Volonteri et al. 2008; Treister et al. 2013; Pacucci et al. 2018; Inayoshi et al. 2020). One of the most commonly used lines in the local universe to this end is Hα (Reines & Volonteri 2015; Baldassare et al. 2016), since it is about three times more intense than Hβ, and it

---

[47] The FIRE/BASS sample shows a higher detection rate of hidden BLRs compared to the other two BASS works, even though it is consistent within ≲2σ given the Poissonian uncertainties. This might be caused by the higher resolving power of this work (R ∼ 6000) with respect to the BASS DR1 (most observations have R = 800, Δv = 375 km s^{-1}, see Table 4 in Lamperti et al. 2017) and with the better observing conditions, resulting in slightly higher S/N, of this FIRE data set in comparison to the DR2 (average seeing 0″.7 in the BASS/FIRE sample versus 1″ in the DR2, den Brok et al. 2022).

is in practice the only line available in the rest-frame optical in the case of Sy 1.9.

5.2.1. BLR Velocity Estimates from Hα and Near-infrared Lines

Figure 4 reports the measured broad Hα from BASS DR2 (Mejía-Restrepo et al. 2022) compared to the measured broad NIR lines from BASS NIR DR1, DR2, and FIRE targets, separated into Sy 1–1.5 (blue circles), Sy 1.8 (cyan circles), and Sy 1.9 (yellow circles) where both optical and NIR BLR components are detected. We recall that we consider the collection of reliably detected broad-line measurements as the *NIR* line sample (in *italic*, see footnote in Section 4.2), being the weighted average FWHM in case there is more than one NIR broad-line detection. The sample of reliable NIR, as defined in Section 5.1, and Hα broad lines[48] contains 60, 47, 50, and 86 AGN with He I, Paβ, Paα, and *NIR* broad lines, respectively. The sample with robust optical measurements, i.e., with <10% uncertainty in the measured FWHM Hα, contains 42, 31, 33, and 60 AGN with He I, Paβ, Paα, and *NIR* broad lines, respectively (see black filled squares in Figure 4). The measurements show some dispersion around the one-to-one locus, with the Paschen-line FWHM being on average higher than the Hα one, which might be driven by the less extincted view in the NIR with respect to the optical band; though the averages velocities measured from Hα and all the NIR lines considered are consistent (<1σ) within the uncertainties of the mean (see Table 2).

We found that for the whole sample (see "all" in Table 2), the Pearson coefficients are high (>0.66) and statistically significant, as also confirmed by a Students T-test. This means that the Hα and NIR measurements of the BLR velocities are statistically describing the same velocity field. The intrinsic spreads with respect to the Hα are 0.14, 0.10, 0.15, and 0.13 dex for He I, Paβ, Paα, and *NIR*, respectively. Note that these correlations between optical and NIR broad lines do not depend on our fitting approach, since we are comparing broad lines that come from different spectral regions that are fit independently.

In order to verify whether some particular classes of Sy are strongly influencing the result, we split the sample into Sy 1–1.5 and Sy 1.8–1.9 and compare the more secure optical and NIR detections (i.e., the black symbols in Figure 4 and the "more robust" cases in Table 2). The results are confirmed: the optical and NIR BLR measurements give consistent estimate of the BLR velocity fields. Additionally, the FWHM measured in Sy 1–1.5 versus Sy 1.8–1.9 come statistically from the same parent population in both NIR and optical. Similar statistical conclusions are derived even adopting the Kolmogorov–Smirnov test and a nonparametric test like the Kendall τ and bootstrapping to consider the measured errors on the FWHM (e.g., pymccorrelation python package, Privon et al. 2020). Therefore, we can conclude that once a broad Hα line is securely detected, the Hα width is in agreement within the intrinsic scatter, with the broad-line width as measured in the NIR. This scatter might be partially explained by AGN variability since the spectroscopic measurements of the optical and NIR are often obtained from nonsimultaneous observations.

---

[48] From the BASS Hα DR2 database, we excluded BAT 557 whose observation does not have nightly flux calibrations, thus resulting in higher uncertainties on the flux measurement (e.g., Koss et al. 2017).

Table 2
Statistical Information of the Optical and Near-infrared BLR Velocity Measurements

N	Sample	$\langle$FWHM(Hα)$\rangle$ (km s^{-1})	$\langle$FWHM (He I)$\rangle$ (km s^{-1})	r	$P(r)$
(1)	(2)	(3)	(4)	(5)	(6)
60	all	3872 ± 249	3669 ± 212	0.67	3.4E-09
41	Sy 1–1.5	3665 ± 260	3644 ± 266	0.77	5.1E-09
19	Sy 1.8–1.9	4319 ± 549	3724 ± 356	0.58	9.5E-03
42	all more robust	3942 ± 298	3869 ± 265	0.65	2.9E-06
28	Sy 1–1.5 more robust	3674 ± 275	3853 ± 340	0.75	4.1E-06
14	Sy 1.8–1.9 more robust	4477 ± 701	3900 ± 430	0.64	1.3E-02

N	Sample	$\langle$FWHM(Hα)$\rangle$ (km s^{-1})	$\langle$FWHM (Paβ)$\rangle$ (km s^{-1})	r	$P(r)$
(1)	(2)	(3)	(4)	(5)	(6)
47	all	3176 ± 214	3478 ± 215	0.81	6.4E-12
35	Sy 1–1.5	3117 ± 220	3304 ± 210	0.87	1.0E-11
12	Sy 1.8–1.9	3346 ± 559	3987 ± 571	0.74	6.0E-03
31	all more robust	3157 ± 260	3342 ± 261	0.85	1.2E-09
22	Sy 1–1.5 more robust	3169 ± 254	3285 ± 267	0.87	1.3E-07
9	Sy 1.8–1.9 more robust	3125 ± 673	3480 ± 648	0.84	4.7E-03

N	Sample	$\langle$FWHM(Hα)$\rangle$ (km s^{-1})	$\langle$FWHM (Paα)$\rangle$ (km s^{-1})	r	$P(r)$
(1)	(2)	(3)	(4)	(5)	(6)
50	all	3159 ± 218	3299 ± 235	0.66	1.4E-07
38	Sy 1–1.5	3269 ± 233	3188 ± 272	0.69	1.4E-06
12	Sy 1.8–1.9	2808 ± 539	3650 ± 468	0.71	9.6E-03
33	all more robust	3192 ± 244	3403 ± 313	0.62	1.2E-04
25	Sy 1–1.5 more robust	3320 ± 225	3318 ± 357	0.61	1.1E-03
8	Sy 1.8–1.9 more robust	2792 ± 744	3669 ± 688	0.75	3.1E-02

N	Sample	$\langle$FWHM(Hα)$\rangle$ (km s^{-1})	$\langle$FWHM (NIR)$\rangle$ (km s^{-1})	r	$P(r)$
(1)	(2)	(3)	(4)	(5)	(6)
86	all	3593 ± 192	3467 ± 158	0.73	1.6E-15
58	Sy 1–1.5	3557 ± 199	3358 ± 187	0.83	8.4E-16
28	Sy 1.8–1.9	3669 ± 427	3694 ± 295	0.62	4.0E-04
60	all more robust	3620 ± 232	3486 ± 194	0.75	5.5E-12
40	Sy 1–1.5 more robust	3573 ± 216	3362 ± 227	0.82	6.0E-11
20	Sy 1.8–1.9 more robust	3715 ± 555	3734 ± 365	0.72	3.5E-04

Note. Columns: (1)–(2) sample size and type, (3) average FWHM of the broad Hα, (4) average broad near-infrared line, (5)–(6) Pearson correlation coefficient and probability.

We examine in Figure 5 the difference in the measured BLR velocities as a function of the line-of-sight column density N_H measured in the X-rays (Ricci et al. 2017a). In order to verify the dependencies between the y and x variables, we adopt a standard forward regression using the linmix_err routine of
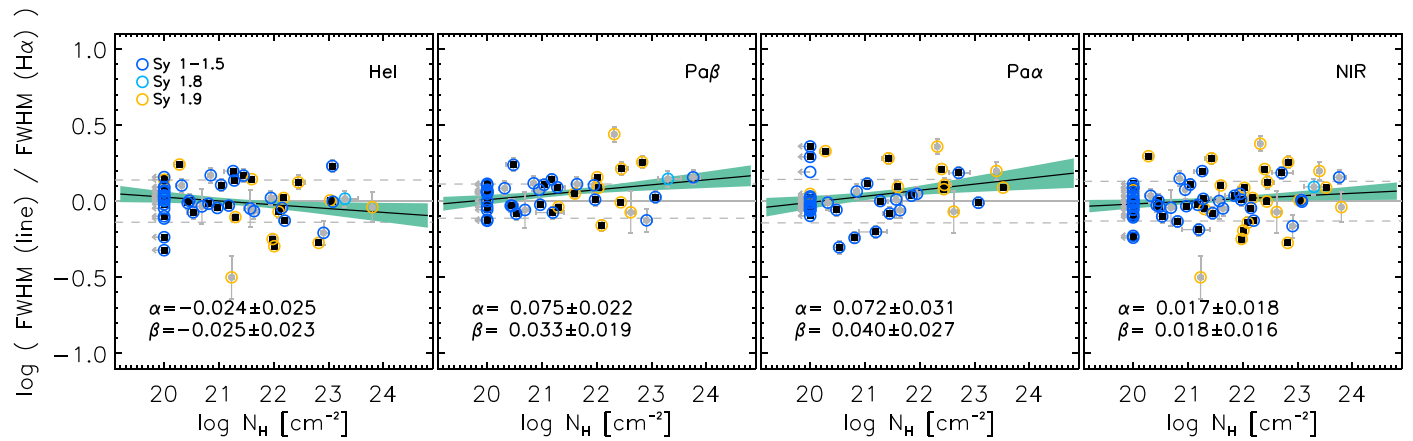
Figure 5. Ratio of the FWHM velocities measured in the NIR to the ones measured from the broad Hα as a function of the line-of-sight X-ray column $N_{\rm H}$. The panels from left to right compare He I, Paβ, Paα, and *NIR*, respectively. Symbols are plotted with the same color scheme as in Figure 4. For each panel, the gray solid line shows where the velocities are equal, and the dashed lines mark the $\pm 1\sigma$ intrinsic scatter. The solid black lines are the best-fit Bayesian relations derived using `linmix_err` together with the 68% c.l. region plotted in green. The best-fit slope β and intercept α with their uncertainties are reported as well. The normalizations y_0 and x_0 in Equation (6) are set to 1 and 10^{22} cm^{-2}, respectively.

Kelly (2007), which employs a fully Bayesian approach, and we fit linear log–log relations

$$\log(y/y_0) = \alpha + \beta \log(x/x_0). \qquad (6)$$

The `linmix_err` routine can include censored data (i.e., upper limits) on the *y*-variable. In our analysis, at all times, the upper limits are on the *x*-variable, being the $N_{\rm H}$. The $N_{\rm H}$ upper limits are objects with $N_{\rm H} < 10^{20}$ cm^{-2}, so lacking evidence of absorbing columns in the broad-band X-ray spectral analysis (see BASS X-ray DR1; Ricci et al. 2017a). These objects should, in principle, have at least some obscuration along our line of sight coming from their host galaxy, but it is impossible to detect because of the intervening obscuration in the Milky Way. We adopt as minimum $N_{\rm H} = 10^{19}$ cm^{-2} (Ryan-Weber et al. 2003; Güver & Özel 2009; Treister et al. 2009), treating the $N_{\rm H}$ upper limits as measurements at $N_{\rm H} = 10^{20}$ cm^{-2} with an uncertainty of $\log N_{\rm H} = 1$ dex.

In all the subsamples inspected, the Bayesian best-fit linear regressions (solid black lines in Figure 5 with the 1σ c.l. regions in green) are rather flat, indicating no significant effect of $N_{\rm H}$ on the difference in the line widths due to $N_{\rm H}$. We note that the best-fit slope β found for He I has an opposite sign than what is found for the Paβ and Paα samples, though all slopes are statistically consistent with zero (p-value > 0.1). The reason for this might be the ionization structure in the BLR, since the ionization potential of He I is much higher (≈ 6 times) than that of Paα, Paβ, and Hα. We can conclude that there is a lack of correlation between the NIR-to-optical BLR velocity measurement ratio and the column density $N_{\rm H}$, at least until $N_{\rm H} \simeq 10^{23}$ cm^{-2}. At higher $N_{\rm H}$, the sample is too small to derive meaningful conclusions. This result nicely complements what can be seen using the larger statistical sample of optical BASS DR2 (Mejía-Restrepo et al. 2022) having both Hα broad line and $N_{\rm H}$ measurements (Ricci et al. 2017a). In particular, the FWHM(Hα)–$N_{\rm H}$ plane shows a decrease in the optical Hα width in Sy 1.9 at $N_{\rm H} > 10^{23}$ cm^{-2}; while below this column density, the FWHM-$N_{\rm H}$ distribution is rather flat (see, e.g., their Figure 9).

Observationally, the line-of-sight X-ray column density $N_{\rm H}$ has shown a correlation with occultation events in the X-rays, due to gas clumps located in a dust-free region or at the inner

edge of the dusty torus (see, e.g., Risaliti et al. 2007, 2011; Maiolino et al. 2010; Markowitz et al. 2014; Ricci et al. 2016; Zaino et al. 2020). More prevalent eclipsing events are linked to higher covering factors, placing at least some of the X-ray obscuring material in the dust-free BLR (see also Schnorr-Müller et al. 2016). In fact, Gandhi et al. (2015) have argued that narrow iron Kα line-emitting material could reside in between the BLR and the putative dusty torus. In addition, some works have suggested that the accretion disk could partially contribute to the observed column density in Compton-thick AGN, as they have large inclination angles (e.g., Masini et al. 2016; Ramos Almeida & Ricci 2017). Those observations imply the presence of gas inside the sublimation radius. However, the X-ray column density $N_{\rm H}$ is a line-of-sight local measurement, which is very unlikely to strongly obscure the full BLR. Therefore, we calculated the optical-to-NIR broad-line flux ratios as a way to measure the extinction experienced by the broad Hα with respect to the broad NIR emission lines. Figure 6 shows only a mild trend, statistically consistent with being flat given the dispersion (p-value > 0.05), when comparing the BLR velocity ratio with the broad Hα to NIR broad-line fluxes.

From Figures 5 and 6, we can then conclude that neither the X-ray obscuration nor the BLR extinction significantly affect the measurement of the width of the broad Hα line and of the NIR broad lines, at least among the total local hard X-ray-selected AGN sample up to columns $N_{\rm H} \simeq 10^{23}$ cm^{-2}, once the broad Hα line detection is secure.

5.2.2. Hα Line Intensity Suppression with N_H in Sy 1.9

Rather than affecting the width of the Hα broad line, increasing obscuration might simply diminish the entire line intensity, and therefore the flux, of the broad Hα. Such line suppression would preferentially affect the rest-frame optical lines more than the NIR broad lines. Figure 7 investigates whether there is an increasing trend between the optical/NIR BLR extinction and X-ray column obscuration. This correlation is only marginally significant for the Paα sample (p-value $\lesssim 0.05$), while it is not significant for the He I and Paβ (p-value > 0.10 for both). We find similar results employing the bootstrapping and point perturbation method with the
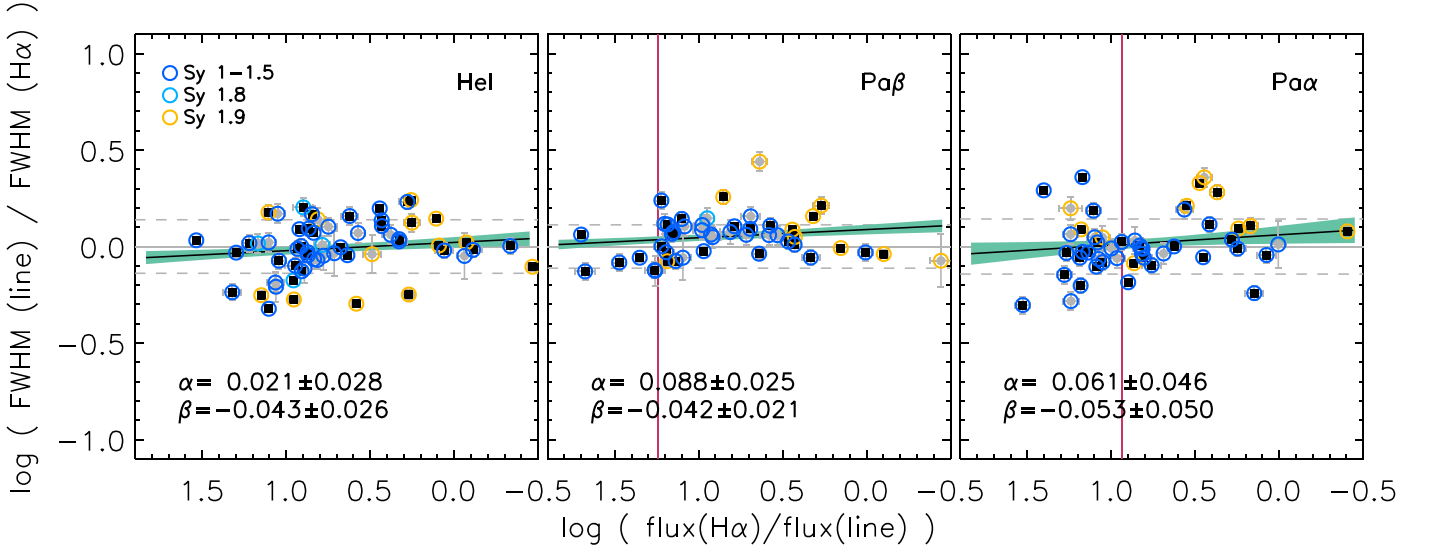
Figure 6. Ratio of the FWHM velocities measured in the near-infrared to the ones measured from the broad Hα as a function of the broad line-flux ratios Hα to near-infrared. The x-axis has been plotted showing the direction of increasing extinction (toward the right). The panels from left to right compare He I, Paβ, Paα, respectively. Symbols are plotted with the same color scheme as in Figure 4. For each panel, the gray solid line shows the locus where the velocities are equal, and the dashed lines mark the ±1σ intrinsic scatter. The solid black lines are the best-fit Bayesian relations derived using `linmix_err` together with the 68% c.l. region shown in green. The best-fit slope β and intercept α with their uncertainties are reported as well. The normalizations y_0 and x_0 in Equation (6) are both set to 1. The red line in the center and right panels is the value of the flux ratios expected assuming case B recombination (see text for more details).
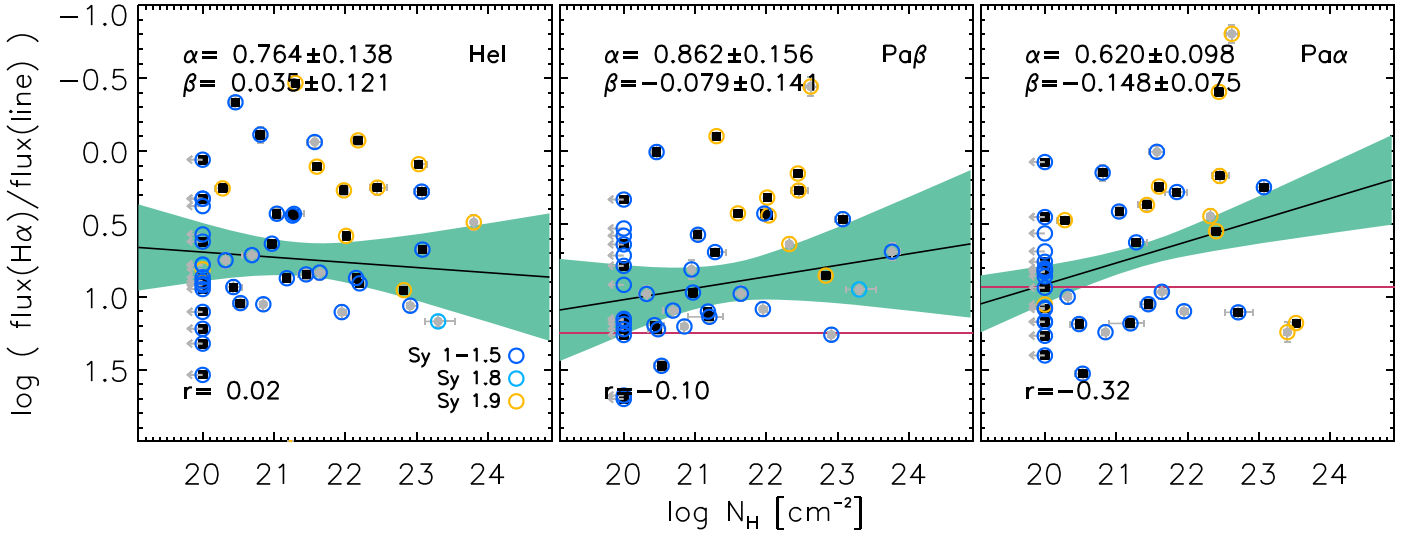
Figure 7. Ratio of the broad-line fluxes measured from Hα and NIR lines He I (left), Paβ (center), and Paα (right) as a function of the line-of-sight X-ray column density (Ricci et al. 2017a). The y-axis has been plotted showing the direction of increasing extinction (toward the top). Symbols are plotted with the same color scheme as in Figure 4. The solid black lines are the best-fit Bayesian relations derived using `linmix_err` together with the 68% c.l. region shown in green. The best-fit slope β and intercept α with their uncertainties are reported as well. The normalizations y_0 and x_0 in Equation (6) are set to 1 and 10^{22} cm^{-2}, respectively. The red line in the center and right panels is the value of the flux ratios expected assuming case B recombination (see text for more details).

`pymccorrelation` package. This observed trend, though only weakly seen for the Paα, is consistent with results from the BASS optical DR2 (Mejía-Restrepo et al. 2022, see their Figure 8), where the broad Hα to 14–150 keV X-ray luminosity ratio shows a sharp decrease of ≲1 dex at $N_H \gtrsim 10^{22}$ cm^{-2} for Sy 1.9 AGN, while this ratio remains rather constant up to $N_H \approx 10^{23}$ cm^{-2} for Sy 1–1.5 types.

A trend of increasing Hα line suppression as a function of N_H implies that M_{BH} measurements based on the Hα broad-line luminosity is biased in the presence of obscuration. Figure 8 shows the ratio between the virial (i.e., $f_0 = 1$) Hα-based BH mass, $[M_{vir,Hα} = M_{vir}(FWHM(Hα), L_{Hα})]$, and the virial NIR+$L_X$-based BH mass for each NIR line, $[M_{vir,line} = M_{vir}(FWHM(line), L_X)]$,

as a function of the X-ray obscuration (left) and broad-line flux ratios, used as a proxy for the BLR extinction (right). The difference between the BH mass estimates increases with increasing obscuration and extinction, more prominently for Sy 1.9 AGN, indicating that the Hα-based BH mass is biased low in the presence of obscuration. The trend expected if the NIR-based BH mass was underestimating the true virial M_{BH} at a given Hα-based BH mass would be positive with increasing N_H and increasing BLR extinction, while the opposite trend is observed.

By dividing the sample in two bins of obscuring columns and running a Students T-statistic test on the values in the two bins, we find a statistically significant decrement of
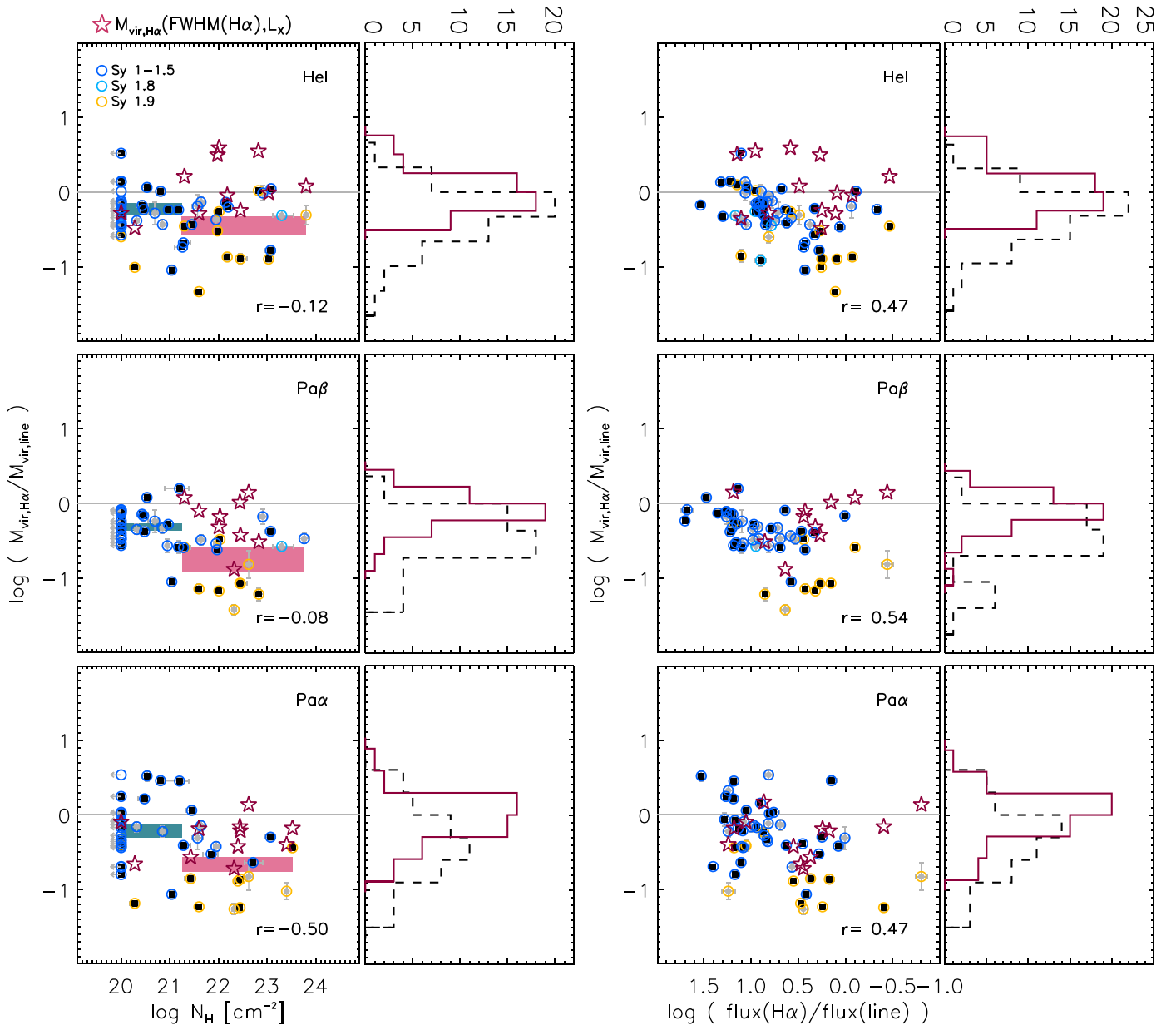
Figure 8. Difference between the virial BH mass estimates from the optical and NIR as a function of obscuration (left) or broad-line fluxes (right), proxy for the BLR extinction. As previously done in Figures 6 and 7, the x-axes in the right panels show the direction of increasing BLR extinction (toward the right). Each row reports a NIR line, from top to bottom: He I, Paβ, and Paα. Symbols are plotted with the same color scheme as in Figure 4. The gray solid lines mark the identity relation. The shaded rectangles in the left panels show the average BH mass difference (together with the error on the mean) computed in two bins of $N_{\rm H}$, low $N_{\rm H}$ in green and high $N_{\rm H}$ in magenta. Red stars show the difference between the BH mass measurements for Sy 1.9 when the $M_{\rm vir,H\alpha}$ is estimated using the same prescription as in the NIR, which is to use the hard X-ray luminosity instead of the Hα broad-line luminosity. The vertical panels show the histograms of the BH mass difference in the case of completely Hα-based (black dashed histogram) or when the hard X-ray luminosity is adopted instead of the broad Hα line luminosity (solid red histogram). In the latter case, the distribution of the mass difference is more consistent with scatter around zero.

$\Delta = 0.23 \pm 0.14$ $(0.44 \pm 0.17, 0.46 \pm 0.13)$ dex with p-value of 4×10^{-2} $(1.7 \times 10^{-4}, 1.3 \times 10^{-3})$ in the BH mass difference between Hα and He I (Paβ, Paα) in the two groups at low and high $N_{\rm H}$. There is a significant bias when the Hα broad-line luminosity is used in SE BH mass estimates in the presence of obscuration $N_{\rm H} > 10^{21}$ cm^{-2}, as can bee seen in the two shaded bins in the left panels of Figure 8 that report the average BH mass difference in the $N_{\rm H}$ bin together with the uncertainty on the mean. Indeed the presence of a bias for the Hα-based BH masses can be seen in the dashed black histogram of the BH mass differences, which are skewed to high (negative) values.

When the same prescription is adopted to measure the optical BH masses, i.e., using the hard X-ray luminosity instead of the broad Hα luminosity as a proxy of the BLR radius (see the red stars for Sy 1.9), the difference between the BH masses derived in the optical and NIR is consistent with scatter around zero offset (see red solid histograms in Figure 8), with no obvious trend versus obscuration or BLR extinction. Therefore, we can conclude that a mixed BH mass estimate based on the hard X-ray luminosity, as put forward by Ricci et al. (2017c; see also Bongiorno et al. 2014; La Franca et al. 2015), can overcome the biases due to extinction and obscuration of the optical Hα broad line in Sy 1.9 and in galaxy-dominated AGN,

where the UV/optical continuum emission can be diluted by the host starlight. Whereas, as long as a broad line is reliably detected and the hard X-ray luminosity is higher than what is expected from the emission coming from X-ray binaries and hot extended gas in the host galaxy, the mixed BH mass estimator can be used to get an unbiased BH mass measurement. We note that adopting L_X instead of the UV/optical luminosity may introduce a weak dependence on M_{BH} and/or L_{Edd} (see Lusso et al. 2010; Liu et al. 2021, albeit there is significant scatter in the correlations). However, the extremely tight ($\sim$0.2 dex) nonlinear L_X–L_{UV} relation has been extensively used to compute Hubble diagrams for quasars, after accounting for flux-limit-related biases and testing for additional systematics (Lusso et al. 2020, and references therein). Further investigation on possible L_{Edd} dependencies will be addressed in a forthcoming paper (F. Ricci et al. 2022, in preparation).

5.3. Dust Extinction toward the BLR and Gas Absorption in the X-Rays

The central and right panels of Figures 6 and 7 report the expected value of the Hα/Paβ and Hα/Paα flux ratio for case B recombination at $T = 10^4$ K and $n = 10^6$ cm^{-3} (Osterbrock & Ferland 2006). We see a wide range of these ratios, with the Paschen lines ruling out case B recombination in most of the X-ray obscured objects (see also Soifer et al. 2004; Glikman et al. 2006; Riffel et al. 2006; La Franca et al. 2015).

If anyhow we assume that the Paschen lines respect the case B recombination, we can use those broad-line flux ratios to quantify the amount of extinction toward the BLR A_V(BLR). Then we could check whether the decline by dust extinction observed in Figure 7 is consistent with the gas absorption, by assuming the Galactic dust-to-gas ratio.

We compute the dust extinction toward the BLR A_V(BLR) following (Domínguez et al. 2013, see their Equation (3)): we assumed the reddening curve $k(\lambda)$ from Calzetti et al. (2000), and that the relationship between the nebular emission-line color excess and the Paschen-to-Hα decrement is given by

$$E(B - V) = \frac{E(\text{H}\alpha - \text{Pa})}{k(\lambda_{\text{H}\alpha}) - k(\lambda_{\text{Pa}})}$$

$$= \frac{2.5}{k(\lambda_{\text{H}\alpha}) - k(\lambda_{\text{Pa}})} \log\left[\frac{(\text{Pa}/\text{H}\alpha)_{\text{obs}}}{(\text{Pa}/\text{H}\alpha)_{\text{case B}}}\right] \quad (7)$$

where $E(\text{H}\alpha - \text{Pa})$ is the $E(\text{H}\alpha - \text{Pa}\beta)$ and $E(\text{H}\alpha - \text{Pa}\alpha)$ excess, the $k(\lambda_{\text{H}\alpha})$ and $k(\lambda_{\text{Pa}})$ are the Calzetti et al. (2000) reddening curve evaluated at the Hα, Paβ, and Paα wavelengths, and (Pa/Hα) are the broad-line flux ratio Paβ/Hα and Paα/Hα. We also assume that A_V(BLR) = $3.1 \times E(B - V)$. We then calculate the $A_V(N_H)$ from the Galactic dust-to-gas ratio, $N_H/A_V = 2.69 \times 10^{21}$ cm^{-2} (Nowak et al. 2012). The comparison between the two independent A_V estimates is presented in Figure 9. Figure 9 shows a separation with Seyfert subclasses: most of the Sy 1s lie above the 1:1, thus the $A_V(N_H)$ is somewhat underestimating the BLR extinction, whereas Sy 1.9s have A_V(BLR) $\sim$ 1–5, and their A_V(BLR) are mostly below the 1:1, thus the A_V derived from dust extinction is less than what is expected from gas absorption. This result is in agreement with what has been found in Shimizu et al. (2018, see their Figure 13), where the A_V(BLR), estimated from the broad Hα-to-hard X luminosity ratio, in Sy 1.9 is lower than what is expected from the Galactic
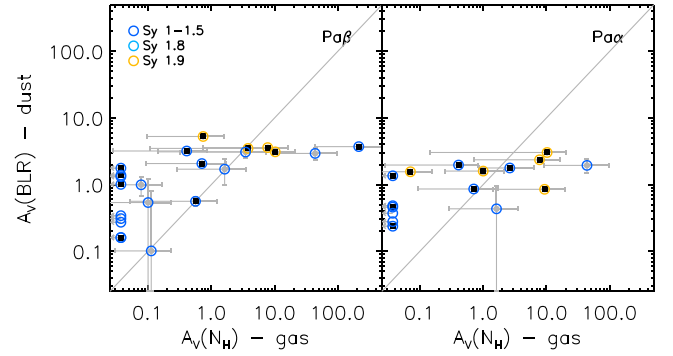

Figure 9. Comparison between A_V expected from gas absorption and A_V toward the BLR due to dust extinction, computed from the broad-line flux ratio of Paβ (left) and Paα (right) to Hα. Symbols are plotted with the same color scheme as in Figure 4. The 1:1 is shown in solid gray.

dust-to-gas ratio, particularly for A_V(BLR) > 3. We note that we adopt a single Galactic dust-to-gas ratio of 2.69×10^{21} cm^{-2}, while in the literature it spans a range from 1.79×10^{21} cm^{-2} (Predehl & Schmitt 1995) to the value we assume. Furthermore, there is evidence that in AGN the dust-to-gas ratio is not Galactic (Maiolino et al. 2001). If we adopt the average dust-to-gas ratio from Maiolino et al. (2001), e.g., 1.1×10^{22} cm^{-2}, then the derived $A_V(N_H)$ would be a factor $1.1/0.269 \simeq 4.1$ smaller than what is shown in Figure 9.

Figure 9 suggests that the extinction toward the BLR and line-of-sight X-ray N_H are distinct, i.e., they are due to a separate obscuration medium. This difference might arise because the BLR extinction is a *global* diffuse measurement while the N_H is a more *local* line-of-sight measurement, or if there is gas within the BLR. Alternatively, it might suggest that the dust-to-gas ratio is somehow different from the Galactic value for BASS AGN. Given the large spread in Galactic dust-to-gas ratio and the uncertainty in what is the A_V/N_H in AGN environments, we cannot distinguish between these two possibilities.

5.4. Near-infrared Line Suppression with Obscuration in Sy 1.8–1.9–2 Types?

We might then ask whether the same effect of line luminosity suppression is similarly experienced by Paschen and helium lines in the NIR as observed for the broad Hα line. Figure 10 shows the ratio of the broad Hα (left) and NIR emission lines to the BAT 14–195 keV hard X-ray luminosity as a function of the X-ray column density for all BASS targets with reliable NIR broad-line detections and with the available N_H. There is a decreasing trend of the NIR to X-ray luminosity ratio with increasing X-ray obscuration, as similarly observed for the Hα. Binning the data in quantiles of log N_H and splitting the sample into Sy 1–1.5 (black squares) and Sy 1.8–1.9-2 (dark-red squares), Sy 1–1.5 AGN exhibit a roughly constant average $L(\text{line})/L_X$ across the N_H range probed by our sample, while the $L(\text{line})/L_X$ of Sy 1.8-.9-2 types seems to decrease as N_H grows. This effect seems particularly more prominent at shorter wavelengths. Running a Student's T-statistic test, we find a statistically significant decrement of $\Delta = 0.54 \pm 0.15$ (0.54 ± 0.12, 0.46 ± 0.14, 0.27 ± 0.12) dex with p-value of 6.8×10^{-6} (4.9×10^{-5}, 2.1×10^{-3}, 3.3×10^{-2}) in the Hα (He I, Paβ, Paα) to hard X-ray luminosity ratio between the two groups divided at $\log(N_H/\text{cm}^{-2}) = 21.25$ (21.75, 21.45,
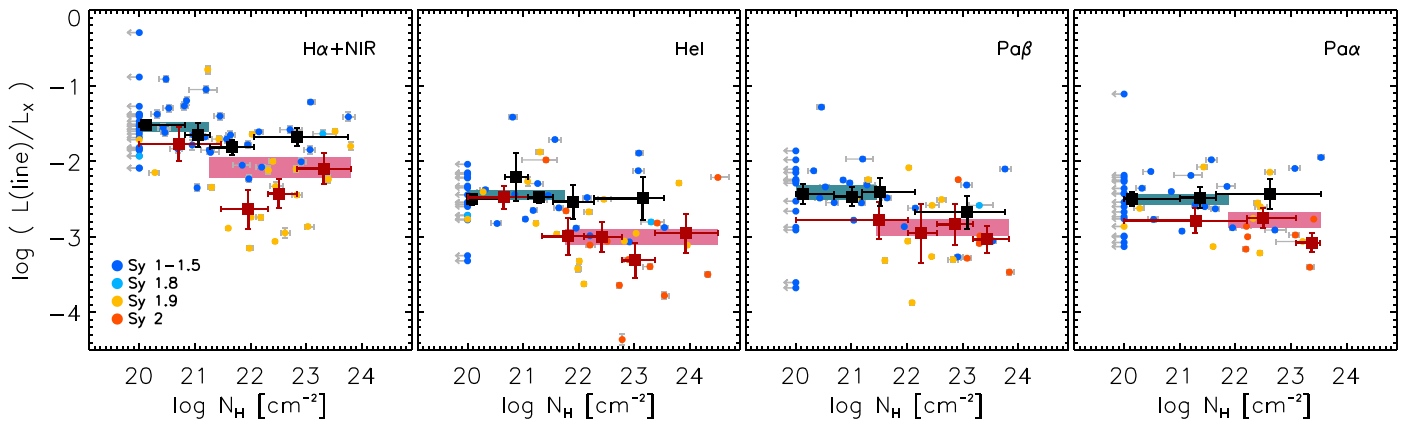
Figure 10. Ratio of the broad-line luminosities to the BAT 14–195 keV hard X-ray luminosities, from left to right: Hα, He I, Paβ, and Paα. The Hα measurements are BASS targets with robustly detected NIR and Hα broad lines (the Hα+NIR is thus only a subsample of the BASS DR2; see, e.g., Mejía-Restrepo et al. 2022). Symbols are plotted with the same color scheme as in Figure 4, with the addition of Sy 2 as red circles. The dashed areas show the average luminosity ratio (together with the error on the mean) computed in two bins of N_H, low N_H in green and high N_H in magenta (see text for more details). The filled squares are the averages in quantiles of $\log N_H$ for Sy 1–1.5 (black) and Sy 1.8–1.9–2 (dark red), with bars reporting the error on the mean of the luminosity ratio and the bin size in $\log N_H$.

21.85), as can be seen in the two shaded rectangles in Figure 10 that report the average luminosity ratio in the two N_H bins together with the uncertainty on the mean. The decrement observed in the Hα to X-ray luminosity can explain the bias observed in Figure 8. We note that the decrement in the Hα to X-ray luminosity happens at a column density level that is slightly lower than what observed in the other NIR lines, which might be explained considering that dust attenuation diminishes when moving to longer wavelengths. NIR line luminosity, when available, should be preferred to the Hα broad-line luminosity as a proxy for the BLR radius when estimating M_{BH} using SE techniques.

Finally, the last question we ask is the following: is NIR really penetrating into the BLR, or is the NIR BLR velocity estimate as good as the Hα (e.g., see Figures 4, 5, and 6) just because both are biased in the same way with increasing column density? Figure 11 can help address this, showing the FWHM–N_H plane for all the BASS Sy AGN having the reliable NIR broad-line detection and available N_H. The Hα BLR velocity estimate is also reported for the subsample of the optical BASS DR2 with N_H and both NIR and Hα reliable broad-line detections. When binning in quantiles in $\log N_H$, the average FWHM measured in the NIR in Sy 1.8–1.9-2 remains quite constant across the N_H range, with only a slight decrease in the highest N_H bin ($\log(N_H/cm^{-2}) \gtrsim 23.5$); the error bars are fully consistent with a constant trend versus obscuration. This behavior is in agreement with the results presented in Onori et al. (2017b), who used a much smaller sample of local hard X-ray BAT-selected obscured AGN ($N = 17$). Also among Sy 1–1.5 types, the average FWHM is rather constant, given the uncertainties, until $\log(N_H/cm^{-2}) \simeq 22$; while in the last N_H bin, there is an upturn. We note that a similar behavior is observed as well in the optical BASS DR2 in the FWHM(Hβ)–N_H plane (see Figure 9 of Mejía-Restrepo et al. 2022). This upturn behavior in Sy 1–1.5 might be related just to small sample statistics, since type 1 AGN with high N_H are quite rare. However taken at face value, we can speculate that it might be related to a transition in Sy type when the FWHM is smaller than 4000 km s^{-1} and $N_H \gtrsim 10^{22}$ cm^{-2}. At high X-ray columns and high inclinations, the optical photons might in some cases still find their way through the obscuring medium by experiencing multiple scatterings. If this hypothesis were plausible, the fraction of optical polarized light in this particular

sample of Sy 1 with high N_H should be higher than what is usually found in normal Sy.

From Figures 10–11, we conclude that (1) the Hα and NIR FWHMs are not affected by obscuration, at least up to $\log(N_H/cm^{-2}) \approx 23.5$, and (2) the NIR line luminosities are not as strongly extincted as the Hα and can be used in SE BH mass measurements until $\log(N_H/cm^{-2}) \approx 21.5$–22, depending on the specific line chosen.
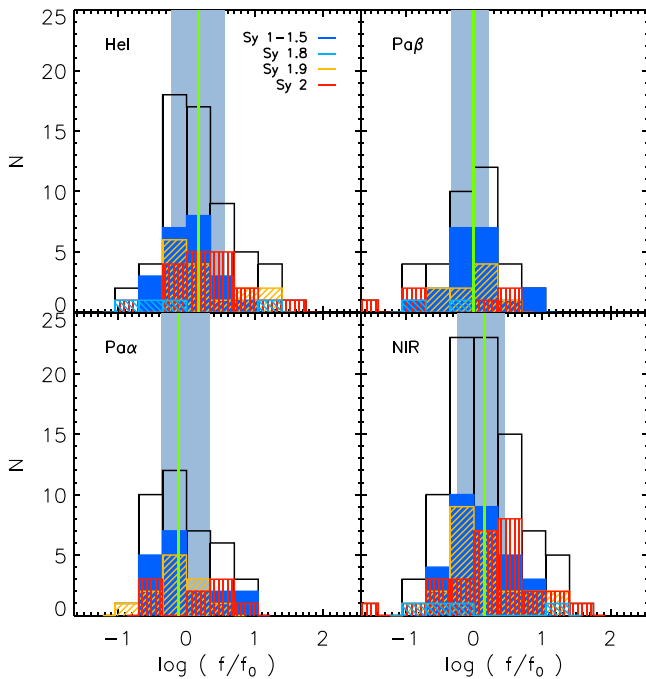
5.5. The Virial Factor f

We finally verify if the BH mass estimates obtained from two independent methods, i.e., the NIR+L_X-based BH mass M(line) and the $\sigma_\star$-based BH mass $M_{BH,\sigma_\star}$, are consistent and, if not, what the quantities are that possibly drive the difference.

The resulting sample is composed of 60, 37, 39, and 88 local BASS Sy having optical $\sigma_\star$ (T. Caglar et al. 2022, in preparation; Koss et al. 2022) and He I, Paβ, Paα, and NIR robustly detected broad lines available, respectively. We were able to gather optical $\sigma_\star$ measurements inside BASS DR2 for ~62%–68% of the sample with NIR broad-line detections, as there are only 30, 23, 24, and 41 sources without available optical $\sigma_\star$ for the He I, Paβ, Paα, and NIR sample, respectively. We show in Figure 12 the histograms of the normalized virial factor f/f_0, which is basically the ratio $M_{BH,\sigma_\star}/M$(line). Each panel reports the distribution of f/f_0 separately for each line subsample, color-coded according to the Sy classification as shown in the legend. The vertical green line marks the 50th percentile, and the shaded area encloses the 25th to 75th percentiles of the whole sample (black histogram), also known as interquartile range IQR. The histograms are all roughly centered around 0, meaning that the normalized virial factor is of the order of unity, with a distribution ranging from −1 to 1. Some sources show high f/f_0 values, e.g., $1 < \log f/f_0 < 2$ and $-2 < \log f/f_0 < -1$, being considered as outliers. These sources have the ratio of BH masses deviating from each other more than one order of magnitude. We discuss the possible reasons why these sources are outliers in Appendix B. In all the subsequent analysis and plots, these most deviating objects are reported as black crosses, and are omitted when performing linear regression fits. Table B1 lists the broad-line measurements of the samples and ancillary quantities.
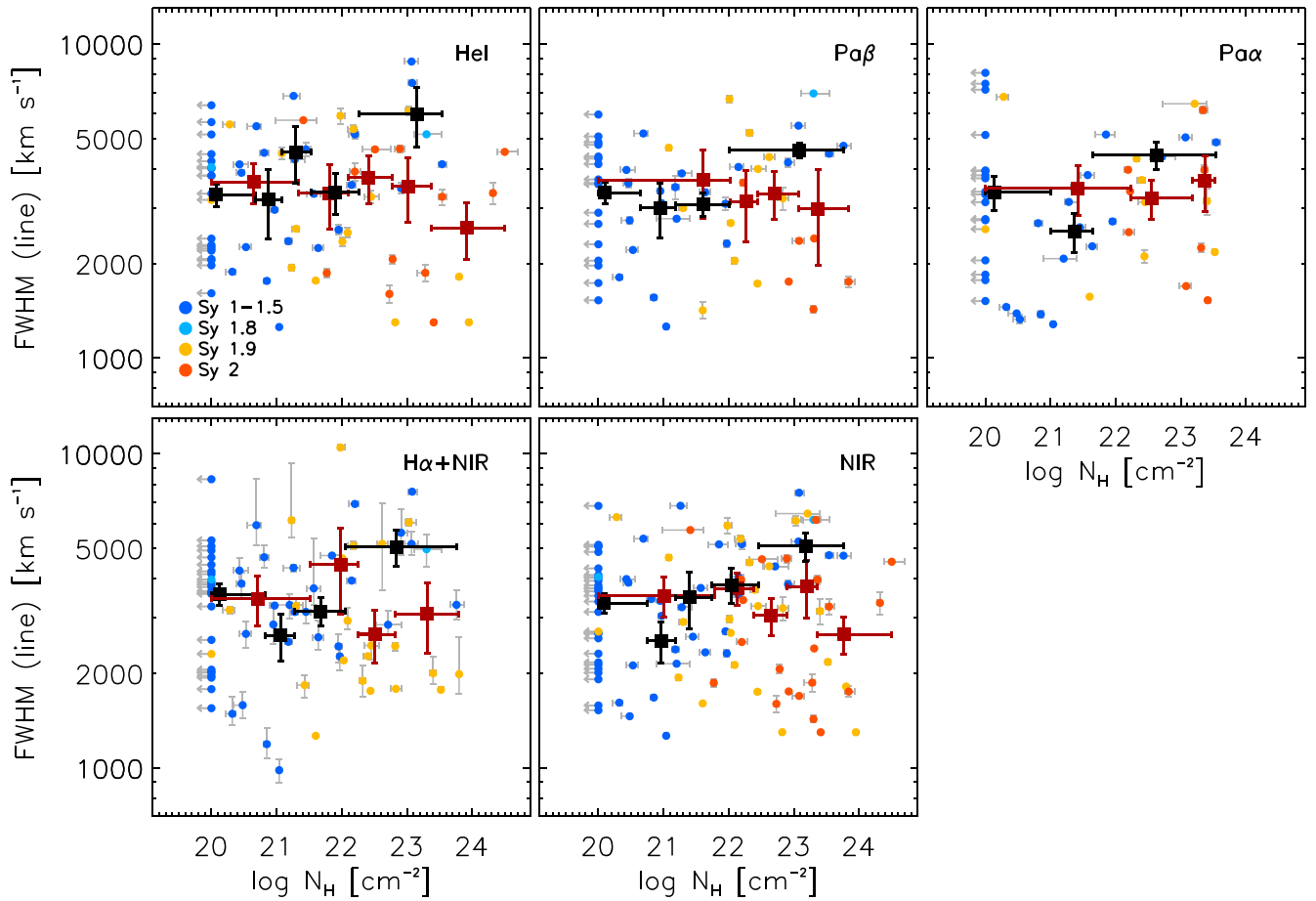
Figure 11. The FWHM–N_H plane for BASS AGN having reliable, broad detected NIR lines as reported in the labels. Symbols plotted as in Figure 10.


Figure 12. Histograms of the normalized virial factor f/f_0, i.e., BH mass deviation $M_{BH,\sigma_\star}/M$(line), for each line subsample, as labeled in each panel. Total sample in black, Sy 1–1.5 in blue, Sy 1.8 in cyan, Sy 1.9 in orange, and Sy 2 in red. The shaded area defines the *IQR*, which is the region enclosing the 25th to the 75th percentile of the total distribution. The 50th percentile is overplotted with a solid green vertical line.

In Figure 13, we compare $M_{BH,\sigma_\star}$ and M(line). The panels show separately the BH mass comparison for each reliably detected line, e.g., He I (top-left panel), Paβ (top-right panel), Paα (bottom-left panel), and the average *NIR* FWHM (bottom-right panel). The sample is divided according to Sy classification. Each panel also shows the sample color-coded according to the measured broad FWHM of each considered line. The measurements are evenly distributed around the 1:1 relation (solid gray line in Figure 13) with some intrinsic scatter of ~0.4–0.57 dex (marked with dashed lines in the figure).

As can be seen from the color gradient in Figure 13, some of the scatter between $M_{BH,\sigma_\star}$ and M(line) estimates might be driven by the observed FWHM; smaller FWHMs (lighter pink) are located above the 1:1 locus while broader lines (darker red) are below it. This difference in the BH mass estimates, i.e., the virial factor *f*, is expected in case the FWHM gets broadened with inclination (see, e.g., Collin et al. 2006; Decarli et al. 2008; Shen & Ho 2014; Mejía-Restrepo et al. 2018).

We now investigate whether the scatter between the two different mass estimates depends on additional variables by examining the ratio between the two mass estimates, $M_{BH,\sigma_\star}/M$(line), as a function of either redshift (left panels in Figure 14), X-ray column N_H (center panels in Figure 14), or BH mass estimate based on the virial assumption M(line) (right panels in Figure 14). In all panels, the solid gray line shows the 1:1 zero-point, and the dashed gray lines are indicating the $\pm 1\sigma$ scatter computed earlier. Color bars in each panel show the values of $M_{BH,\sigma_\star}$ (left), M(line) (center), and column density N_H (right) when available. The rows in Figure 14 show f/f_0 for
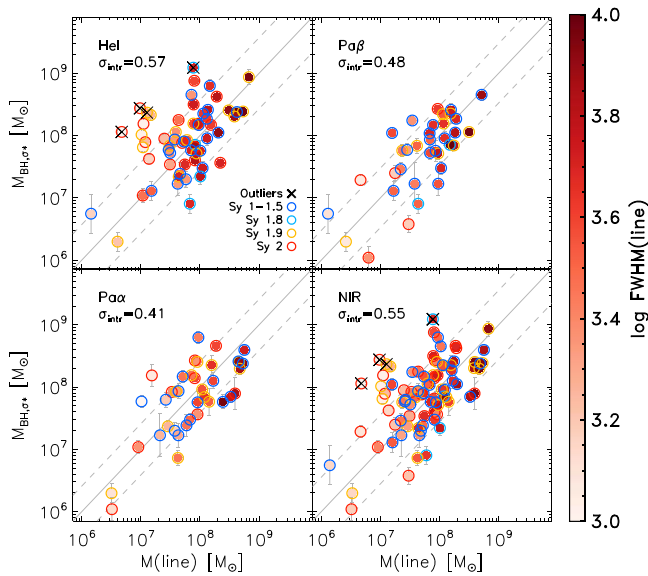
Figure 13. Comparison of $M_{BH,\sigma_\star}$ vs. M(line) in BASS Sy AGN color-coded according to the FWHM(line). The 1:1 relation is shown in solid gray, with dashed gray lines indicating the intrinsic spread. The measurements are evenly distributed around the one-to-one relation, with a clear gradient in FWHM (line): objects with faster BLR velocities are preferentially below the unity locus, while smaller FWHMs are mostly located above the 1:1 relation, in all the lines examined.

each line sample, respectively, from top to bottom: He I, Paβ, Paα, and average *NIR*. In order to quantify the presence of possible correlations between f/f_0 and other physical quantities, we perform a forward regression Bayesian fit as outlined in Equation (6), where x is either redshift, column density, or the NIR+L_X virial-based BH mass estimate M(line), and y/y_0 is f/f_0. Table 3 reports the best-fit parameters obtained using the IDL routine linmix_err, and solid black lines in Figure 14 show the log–log linear best-fit regression with 1σ c.l. In each panel, the Pearson correlation coefficient is also reported.

At fixed aperture, with increasing redshift, a bigger part of the host (bulge) is sampled in 1D spectra, possibly producing an increase on the measured stellar velocity dispersion and therefore an enhancement of $M_{BH,\sigma_\star}$, particularly relevant in late-type systems (Falcón-Barroso et al. 2017). The BAT AGN are typically found in massive spirals with strong bulges (with high concentration index) in between spirals and ellipticals (Koss et al. 2011). As such, the aperture corrections go in different directions, and it is not straightforward to determine what is the appropriate aperture correction to apply (this issue is further explored by T. Caglar et al. 2022, in preparation). Moreover, the line-of-sight velocity dispersion could be broadened due to the disk rotation (Bennert et al. 2011; Har et al. 2012; Kang et al. 2013; Caglar et al. 2020), and this effect should be higher outside the spheroid. In the left panels of Figure 14, we can see that there is no strong gradient of $M_{BH,\sigma_\star}$ along the x-axis, while there is some gradient along the y-axis, meaning that at each redshift there is a range of measured $M_{BH,\sigma_\star}$. This implies that $M_{BH,\sigma_\star}$ has a negligible dependence on redshift. As a matter of fact, the log–log relation (solid black line) always has a flat slope in all cases consistent with zero (see Table 3), and there is no clear correlation between f/f_0 and redshift. Therefore we can conclude that aperture effects are most probably not important for this sample. As a matter of fact, the optical slit width is typically $\approx 1''.5$ in BASS DR2, and at $z = 0.1$, the sampled region would be of

1.85 kpc arcsec^{-1} $\times$ $1''.5 \simeq 2.8$ kpc. The average effective radius in SDSS late-type galaxies (Sa, Sb, Sc) is ~ 2.7 kpc (Oohama et al. 2009); therefore the spectral extraction would still be roughly within the bulge or spheroid, even at the highest redshift probed in this work.

If obscuration was biasing the NIR+L_X virial-based BH masses, the sample should exhibit a gradient with M(line) as a function of the X-ray column, and also we should see a positive correlation between the f/f_0 and the column density. Our sample shows at most the opposite behavior, a mild anticorrelation between f/f_0 and N_H, and no clear gradient in M(line) at increasing N_H (center panels in Figure 14). The derived best-fit relations cannot be statistically distinguished from a relation with a zero slope; thus again there is no statistical evidence for a dependence with X-ray obscuration. This is indeed not surprising since we show in Section 5.4 that the FWHM measured from NIR lines is not affected by obscuration until high X-ray column densities $\log(N_H/\text{cm}^{-2}) \gtrsim 23.5$.

Finally, we explore whether there is an anticorrelation between f/f_0 and M(line), which could be inherited by the adopted definition of f, such that $f \propto M(\text{line})^{-1}$ (we recall that $M(\text{line}) = f_0 \times M_{\text{vir,line}}$, see Section 4.2). The right panels in Figure 14 show that indeed there is an anticorrelation, but the best-fit slopes are always flatter than -1. The correlations between f and M(line) are statistically different from the -1 slope expected simply by definition (see Table 3, p-value $< 7 \times 10^{-8}$), while the statistical dependence is significantly different from a zero slope only in the He I and *NIR* cases. Similar conclusions are reached when bootstrapping and point perturbation analysis are adopted. We note that this $f - M$(line) mild anticorrelation might as well be driven by a more fundamental relation with the FWHM, since $M(\text{line}) \propto$ FWHM(line)^2, and already from Figure 13, it is evident that there is a dependency of the scatter between the two M_{BH} estimates and FWHM. A thorough investigation of the $f -$ FWHM dependence will be carried out in a separate publication (F. Ricci et al. 2022, in preparation).

6. Discussion and Conclusions

In this work, we present 0.8–2.5 μm NIR spectroscopic observations of 65 local BASS selected AGN obtained at Magellan/FIRE, split into 13 Sy 1–1.5 and 52 Sy 1.8–1.9–2 types. We fit four NIR spectral regions (0.9–0.96, 1.04–1.15, 1.15–1.30, and 1.80–2.00 μm) to study the most characteristic NIR BLR properties, i.e., the BLR velocities and radii, estimated from the most prominent NIR hydrogen (Paα and Paβ) and helium (He I 10830 Å) transitions. We combine our NIR FIRE sample with the whole BASS NIR database (DR1; Lamperti et al. 2017; and DR2; den Brok et al. 2022), finding NIR broad emission lines in 64/235 Seyferts 1.8–1.9–2. The results of this analysis confirm the possibility of using the NIR band to probe deeper with the BLR conditions also in optical narrow-line AGN. The line showing the highest success rate of broad-line detection in reddened Seyferts is He I (43/235), followed by Paα (24/235) and Paβ (20/235), suggesting a possible correlation between the NIR line intensity and the higher ability of isolating faint BLR components reliably in Sy 1.8–1.9–2 types.

We then complement the NIR BLR view with the one obtained from the optical, namely the Hα, from BASS DR2 (Mejía-Restrepo et al. 2022). In this way, we constructed the largest NIR sample of hard X-ray-selected local Sy having
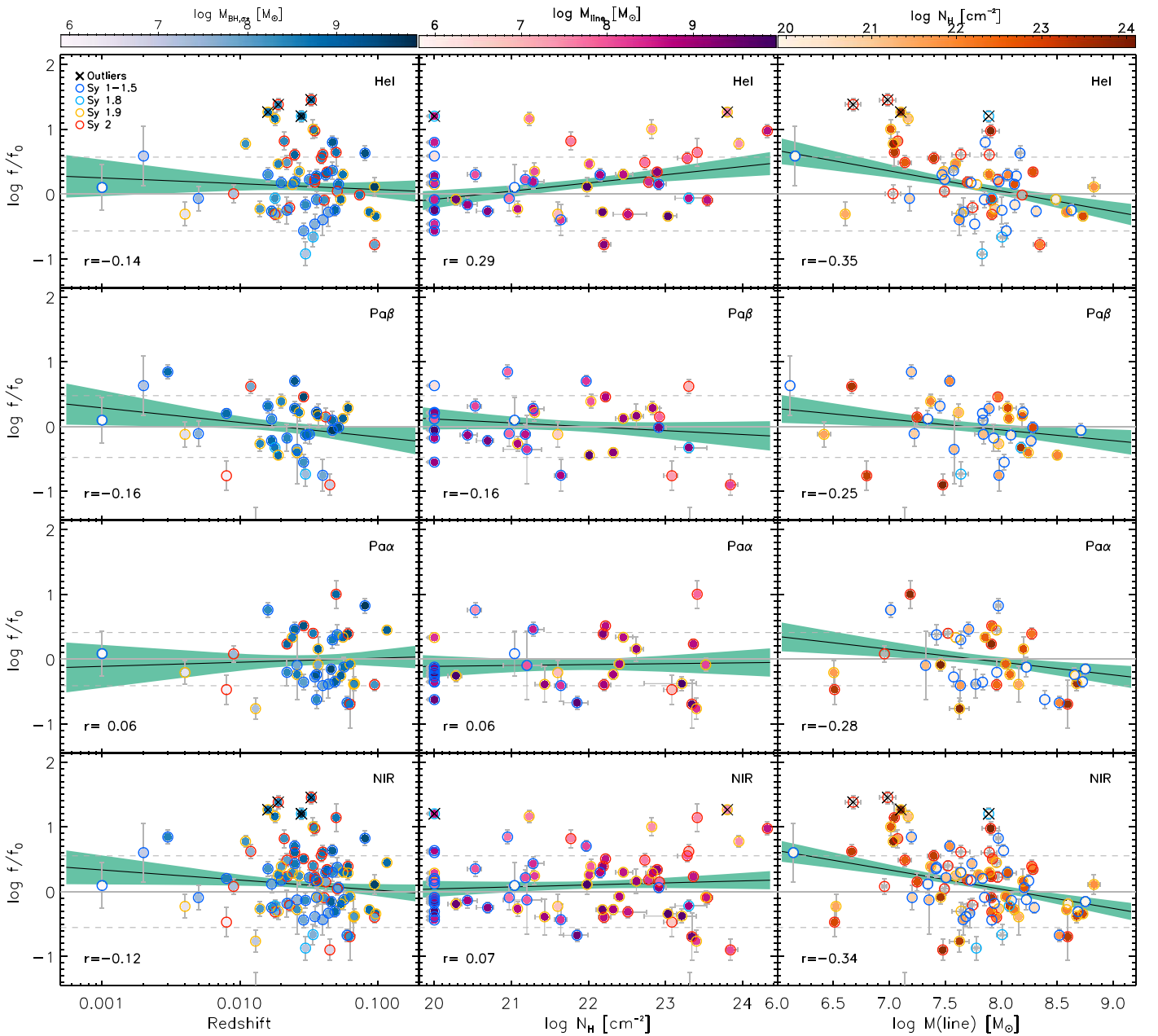
Figure 14. Comparison between the offset $M_{\mathrm{BH},\sigma_\star}/M$(line), i.e., the normalized virial factor f/f_0, as a function of the following: (left) redshift, color-coded with $M_{\mathrm{BH},\sigma_\star}$; (center) N_{H}, color-coded according to M(line); (right) M(line), color-coded according to the N_{H} (when available; if not available, the symbols are gray asterisks). The row shows the sample of each line, from the top: He I; Paβ; Paα; average NIR. The color of the outer circle labels different Sy classes, as reported in the legend. Black crosses mark outliers. Black solid lines refer to log–log linear best-fit regressions, with relative 68% c.l. in green. Pearson correlation coefficients r are reported in the lower left of each panel, see also Table 3.

robust ancillary data available from BASS. In terms of L_X and z, our sample is representative of the BASS AGN sample, even though the fraction of Seyfert types is not (in the BASS DR1 there is an equal portion of Sy 1 and Sy 2; see, e.g., Koss et al. 2017), since our program was aimed at detecting the BLR in the most elusive Seyferts 1.8–1.9–2 (235/314 objects, $\approx$75%).

With this obscuration-unbiased sample in hand, we investigate the presence of possible systematics in the BLR characterization taking advantage of the X-ray, Hα, and NIR spectral information in Sy 1 up to Sy 1.9 (and Sy 2, without the Hα but with NIR broad-line detection). We verify that the FWHM measured from Hα and NIR lines are consistent in Sy 1 up to Sy 1.9. The same results are found even when splitting

the sample according to the Sy subclassification. The Hα and NIR FWHM broad-line measurements statistically describe the same velocity field in the BLR. Thus, once a broad Hα line is reliably detected, its FWHM is in agreement with the NIR FWHM within some scatter ($\approx$0.10–0.15 dex, depending on the specific line). We then demonstrate that the Hα and NIR BLR velocity estimates are not significantly affected by either obscuration or BLR extinction, as measured by the flux decrement of the broad Hα flux to the NIR broad-line flux, at least until $\log(N_{\mathrm{H}}/\mathrm{cm}^{-2}) \approx 23$, as also consistently found in the optical BASS DR2, where the FWHM(Hα)-N_{H} distribution remains constant up to $\log(N_{\mathrm{H}}/\mathrm{cm}^{-2}) \approx 23$ (Mejía-Restrepo et al. 2022).

Table 3
Best-fit Log–Log Linear Regression as Outlined in Equation (6)

Sample	$\log z$				
(1)	α (2)	β (3)	r (4)	$P(r)$ (5)	p-value ($\beta \neq 0$) (6)
He I	-0.02 ± 0.29	-0.09 ± 0.19	-0.14	3.1E-01	6.3E-01
Paβ	-0.38 ± 0.34	-0.22 ± 0.20	-0.16	3.5E-01	2.6E-01
Paα	0.08 ± 0.32	0.06 ± 0.21	0.065	6.9E-01	7.6E-01
NIR	-0.13 ± 0.23	-0.16 ± 0.15	-0.12	2.6E-01	2.9E-01

Sample	$\log \frac{N_{\rm H}}{10^{22}\ {\rm cm}^{-2}}$				
(1)	α (2)	β (3)	r (4)	$P(r)$ (5)	p-value ($\beta \neq 0$) (6)
He I	0.171 ± 0.071	0.127 ± 0.065	0.29	5.6E-02	5.5E-02
Paβ	-0.003 ± 0.081	-0.060 ± 0.081	-0.16	3.6E-01	4.7E-01
Paα	-0.084 ± 0.084	-0.014 ± 0.079	-0.062	7.3E-01	8.6E-01
NIR	0.104 ± 0.058	0.031 ± 0.054	0.066	5.9E-01	5.7E-01

Sample	$\log \frac{M(\rm line)}{10^{7.5}\ M_\odot}$					
(1)	α (2)	β (3)	r (4)	$P(r)$ (5)	p-value ($\beta \neq 0$) (6)	p-value ($\beta \neq -1$) (7)
He I	0.202 ± 0.066	-0.31 ± 0.11	-0.35	7.3E-03	6.3E-03	6.8E-08
Paβ	0.031 ± 0.078	-0.16 ± 0.12	-0.25	1.4E-01	1.8E-01	5.6E-08
Paα	0.053 ± 0.083	-0.20 ± 0.12	-0.28	8.9E-02	9.7E-02	4.0E-08
NIR	0.187 ± 0.053	-0.297 ± 0.088	-0.34	1.5E-03	1.2E-03	9.7E-12

Note. Columns are as follows: (1) sample of each line; (2)–(3) the zero-point and slopes of the best-fit relations; (4)–(5) the Pearson correlation coefficients with the related probability; (6) the probability of the slope being different from zero; (7) same test with the null hypothesis of $\beta = -1$, carried out only for the f/f_0 versus M (line) correlation.

Rather than the Hα FWHM, it is the entire Hα broad-line intensity that gets suppressed with increasing obscuration, implying that the optical Hα photons are obscured by a uniform screen placed outside the BLR. The ratio of broad Hα-to-NIR broad-lines flux shows a mild decreasing trend with $N_{\rm H}$ for the Paα sample, while the statistical evidence is weaker for He I and Paβ. We quantify the amount of dust extinction toward the BLR and the level of gas absorption measured in the X-rays, finding a clear separation in Seyferts subclasses. This has been shown already by several other works (Burtscher et al. 2016; Schnorr-Müller et al. 2016; Shimizu et al. 2018). The comparison of two different A_V estimates suggests that either the material obscuring the BLR is distinct from the one producing the absorption in the X-rays or the dust-to-gas ratio in local hard X-ray-selected AGN environments is not Galactic (see, e.g., Maiolino et al. 2001). There are some limitations in the approach adopted to estimate the A_V(BLR), the most notable being the assumption of case B recombination, which might not hold for Paschen lines (Soifer et al. 2004; Glikman et al. 2006; Riffel et al. 2006; La Franca et al. 2015). Additionally, we stress that the broad-line ratios, Paschen-to-Hα, depend not only on dust extinction but also on collisional effects (i.e., by the ionization parameter U and particle density n) taking place at the high densities of the BLR, $10^{10-11}\ {\rm cm}^{-3}$ (see, e.g., Schnorr-Müller et al. 2016). Therefore the observed dispersion in broad-line flux measurements is likely due to collisional effects in addition to extinction.

We then explore if the line intensity suppression with increasing X-ray column is similarly experienced by NIR line as found in the Hα. We find a decrement in the broad lines to hard X-ray luminosity ratio of 0.54 ± 0.15 dex for Hα, decreasing at longer wavelengths to 0.27 ± 0.12 dex in the

case of Paα, occurring at a level of obscuring column density $\log(N_{\rm H}/{\rm cm}^{-2}) = 21.25$ for Hα, moving to higher $N_{\rm H}$ levels going to longer wavelengths, up to $\log(N_{\rm H}/{\rm cm}^{-2}) = 21.85$ for Paα. The Hα broad-line intensity suppression with increasing $N_{\rm H}$ induces a bias in SE Hα-based BH masses of ≈ 0.2–0.45 dex, depending on the specific line chosen to compare the Hα with. The NIR line luminosity should be preferred to the Hα line luminosities, when available, to estimate $M_{\rm BH}$ using SE relations (Kim et al. 2010; La Franca et al. 2015). Notwithstanding, in the presence of substantial obscuration, $\log(N_{\rm H}/{\rm cm}^{-2}) \gtrsim 22$, the NIR line luminosity can be underestimated, particularly in Sy 1.9–2. Thus to overcome these shortcomings, it is preferable to use a more unbiased luminosity as a proxy to estimate the BLR radius, and a mixed NIR+$L_{\rm X}$ approach as put forward by Ricci et al. (2017c; see also, Bongiorno et al. 2014; La Franca et al. 2015) is a more unbiased estimate of the virial BH mass. The NIR FWHMs seem as well to be much less susceptible to obscuration, at least up to columns $\log(N_{\rm H}/{\rm cm}^{-2}) \approx 23.5$.

We finally evaluate the consistency between $\sigma_\star$-based (from the optical BASS DR2; T. Caglar et al. 2022, in preparation; Koss et al. 2022) and mixed NIR+$L_{\rm X}$ virial-based BH mass estimates, finding that the two quantities agree within ~ 0.4–0.57 dex scatter. The scatter expected in this case is at least the combination of two factors: (i) there is an inherent scatter in the $M_{\rm BH}$–$\sigma_\star$ relation of the order of 0.3 dex, and (ii) the intrinsic scatter of virial-based $M_{\rm BH}$ estimates is $\simeq 0.4$–0.5 dex. Thus, combining the two log-normal contributions, the expected scatter is of the order of 0.5–0.58 dex, which is consistent with what we find. We note however that there are some works suggesting that the $M_{\rm BH}$–$\sigma_\star$ intrinsic scatter might be higher if the host morphology is not properly

taken into account (e.g., Falcón-Barroso et al. 2017); thus we caution the reader that the M_{BH} based on $\sigma_\star$ for single BASS targets might be characterized by a systematic uncertainty >0.3 dex (e.g., Gültekin et al. 2009), as there is an inherent difficulty in applying morphology-based corrections to the BAT AGN sample that is composed primarily by massive spirals and lenticulars with strong bulges, with a high fraction of disturbed mergers (Koss et al. 2010, 2011), adding further complexity to aperture corrections for stellar kinematics.

The ratio of two independent BH mass estimates is here used to derive the virial factor f, for the first time for a less-biased sample, since we also consider the Sy 1.8–1.9–2 showing BLR components in the NIR. The BH–$\sigma_\star$ scaling relation adopted to derive $M_{BH,\sigma_\star}$ is the one proposed by Kormendy & Ho (2013) calibrated for elliptical- and classical-bulges. Still, by normalizing the virial factor f with the ensemble virial factor f_0, we essentially minimize the effects due to the choice of the BH–$\sigma_\star$ scaling relation. As long as the BH–$\sigma_\star$ relation for pseudo-bulges and/or late-type galaxies differs from that of elliptical-/classical-bulges by only a normalization term, as it occurs for the M_{BH}–$\sigma_\star$ relation of pseudo-bulges proposed by Ho & Kim (2014), the different normalization is absorbed in f_0. If instead the M_{BH}–$\sigma_\star$ relation of pseudo-bulges or late-type galaxies has a different slope than the one observed for classical-bulges, then this effect is not absorbed in the f_0 normalization.

Examining the distributions of normalized virial factors f/f_0 divided according to the Seyfert subclassification, our data do not show evidence of different M_{BH} between type 1 and type 2 AGN, as instead claimed by Onori et al. (2017b) and Ricci et al. (2017b). These works used a small sample of BAT-selected local Seyferts 1.8–1.9–2 with NIR broad lines and compare their M_{BH} to the well-known and best-studied BAT-selected type 1 AGN with RM-based BH masses. By matching type 1 and obscured Seyferts in hard X-ray luminosity and stellar velocity dispersion, they find that Sy 1.8–1.9–2 are more undermassive than RM AGN. This BH mass difference is mainly driven by small sample statistics, since (i) their small obscured Seyfert sample do not span the same FWHM range of type 1, being limited to FWHM $\lesssim$ 3600 km s^{-1}, and (ii) the type 1 control sample is biased to higher FWHM, having FWHM $\gtrsim$ 1600 km s^{-1}; while in this work, thanks to the additional spectra obtained with FIRE and Xshooter, we much better populate the FWHM–L_X plane for both AGN populations.

Dependencies of the normalized virial factor f/f_0 with redshift, obscuration, and virial-based BH mass estimate have been explored, only finding a mild dependency with M(line). This mild anticorrelation might be actually due to a more fundamental relation with the FWHM. Indeed, using a sample of about 600 local SDSS optical broad-line AGN, Shen & Ho (2014) show that the virial factor, estimated as $M_{BH,\sigma_\star}/M(H\beta)$, is anticorrelated with the FWHM($H\beta$), and claim that this effect is a by-product of the line broadening due to the inclination of clouds moving in a disk-like BLR (see, e.g., Collin et al. 2006). Similarly, an earlier attempt by Decarli et al. (2008) demonstrated that there is an anticorrelation between the virial factor f, computed as the ratio of the BH mass estimated from the BH-bulge luminosity M_{BH}–L_{bul} relation and the virial $H\beta$-based BH mass, and the broad $H\beta$ FWHM, and this inclination effect might bias SE virial-based BH masses. At higher redshift, using accretion-disk models to get a BH mass estimate independent of the virial assumption, Mejía-Restrepo et al. (2018) have further

demonstrated that this f-FWHM anticorrelation is found not only for the $H\beta$ line but also in $H\alpha$, Mg II, and C IV, and can be explained with inclination effects on the measurements of the velocities of clouds moving in a thin disk BLR. We aim to further investigate this possibility with a more detailed analysis on this issue in a separate paper, exploring possible BLR parameters in space that are consistent with our data (F. Ricci et al. 2022, in preparation).

Our findings corroborate that the use of a mixed virial-based NIR BH mass estimator gives a less-biased view of the BLR properties, and that the use of a single ensemble average virial factor f_0, for the whole AGN population, might bias our understanding about the AGN demographics and evolution, since we showed that f is at least related (though weakly) to M (line) in two broad-line samples (He I and *NIR* line data sets). Hopefully in the near future, the astronomical community will take advantage of the James Webb Space Telescope (JWST), which will essentially allow for the exploration of the rest-frame NIR properties of AGN and galaxies also at higher redshift. Indeed, the Paβ line at $z \sim 2$–3 can be observed in the 1–5 μm wavelength range with NIRSpec on board JWST. Additionally, being a satellite, the limitations due to ground-based observations will be overcome, and more efficient NIR observations will be carried out, opening the path to the construction of large statistical samples of AGN with rest-frame NIR coverage at higher redshifts.

7. Summary

With the largest and least-biased sample of local hard X-ray-selected AGN with rest-frame NIR spectroscopy, we characterize three key BLR properties directly related to virial-based BH mass measurements, i.e., the BLR velocity, estimated from broad-line widths FWHM, the average BLR radius, from broad-line and X-ray luminosities, and from BLR geometry/dynamics, enclosed in the virial factor f. Our findings are the following:

1. The FWHMs measured from $H\alpha$ and NIR broad lines He I, Paβ, and Paα are consistent in Sy 1 up to Sy 1.9, within an intrinsic scatter of 0.10–0.15 dex; thus the optical and NIR statistically describe the same velocity field in the BLR. Moreover, the FWHM measurements do not depend on the level of BLR extinction or X-ray column density, at least up to $\log(N_H/cm^{-2}) \approx 23.5$.

2. The $H\alpha$ broad-line luminosity gets suppressed with increasing obscuration, with a decrement of 0.54 ± 0.15 dex in the $L(H\alpha)/L_X$ ratio occurring at $\log(N_H/cm^{-2}) = 21.25$ cm^{-2}. This effect produce a bias in SE $H\alpha$-based M_{BH} when $N_H \gtrsim 10^{21}$ cm^{-2}.

3. The material obscuring the BLR is distinct from the one responsible for the X-ray absorption, or the dust-to-gas ratio is not Galactic in hard X-ray-selected local Seyfert environments.

4. NIR broad lines are suppressed with increasing obscuration, but the decrement is smaller than the $H\alpha$ broad line (0.54 ± 0.12, 0.46 ± 0.14, and 0.27 ± 0.12 for $L(\text{He I})/L_X$, $L(\text{Pa}\beta)/L_X$, and $L(\text{Pa}\alpha)/L_X$, respectively) and occurs at slightly higher N_H levels, $\log(N_H/cm^{-2}) = 21.75$, 21.45, and 21.85 for He I, Paβ, and Paα, respectively. Even NIR broad-line luminosities should not be used in SE M_{BH} estimates when $N_H \gtrsim 10^{22}$ cm^{-2}, and a less-biased BLR

radius proxy should be used, as the hard X-ray luminosity L_X.

5. Using two obscuration-unbiased BH mass estimates, one based on the $\sigma_\star$ and the other based on the mixed NIR+L_X virial mass, we show that the two BH mass measurements agree with each other with an intrinsic scatter of 0.4–0.57 dex.

6. We quantify the virial factors f as the ratio of these two independent BH mass measurements and verify that Sy 1 and Sy 1.8–1.9–2 types have the same distribution of virial factors and that our virial factors are not biased with z or N_H but show a mild anticorrelation with M(line). This last finding might be driven by a more fundamental anticorrelation with the observed FWHM expected due to inclination effects.

Appendix A
FIRE/Magellan Broad-line Fit Measurements

In this section, we list the spectral emission-line fit measurements of the He I and Paγ (Table A1), Paβ (Table A2), and Paα (Table A3) broad lines for the whole FIRE/Magellan sample. The few cases in which additional components in the Paγ or Paα region were required are presented in Tables A4–A5.

Table A1
Broad-line Measurements of the He I and Paγ

BAT ID	Flag	Noise	He I Flux	Paγ Flux	FWHM He I (km s^{-1})	FWHM Paγ (km s^{-1})	Δv He I (km s^{-1})	Δv Paγ (km s^{-1})
(1)	(2)	(3)	(4)	(5)	(6)	(7)	(8)	(9)
7	2	4.21E-17	<6.00	<2.59				
10	2	1.12E-17	1.968 ± 0.064	<0.65	7072 ± 273		-312 ± 42	
80	2	2.19E-16	<10.91	<5.14				
118	2	1.42E-17	<0.69	<0.75				
238	9	2.45E-17	<0.72	<0.79				
262	4	3.88E-17	<4.61	<2.48				
272	4	4.65E-17	0.92 ± 0.37	1.238 ± 0.082	1302 ± 521	1289 ± 203	1000 ± 232	1000 ± 232
305	2	3.75E-17	1.342 ± 0.028	<2.44	1297.76 ± 0.03		-53.4 ± 6.3	
329	9	4.92E-17	<4.95	<15.78				
372	3	2.91E-17	<4.55	7.44 ± 0.78		11552 ± 306		534 ± 142

Note. Columns: (1) BAT ID; (2) quality fit flag; (3) noise measured in the continuum in erg cm^{-2} s^{-1} Å^{-1}; (4), (6), and (8) He I flux (in units of 10^{-14} erg cm^{-2} s^{-1}), FWHM, and velocity shift, respectively; (5), (7), and (9) Paγ flux (in units of 10^{-14} erg cm^{-2} s^{-1}), FWHM, and velocity shift, respectively. Values in columns (4)–(5) preceded by "<" indicate upper limits. The upper limits on the broad-line fluxes have been computed using a FWHM = 4200 km s^{-1}.

(This table is available in its entirety in machine-readable form.)

Table A2
Broad-line Measurements of the Paβ

BAT ID	Flag	Noise	Paβ Flux	FWHM Paβ (km s^{-1})	Δv Paβ (km s^{-1})
(1)	(2)	(3)	(4)	(5)	(6)
7	4	3.50E-17	<17.87		
10	9	9.81E-18	<13.43		
80	4	1.20E-16	<2.79		
118	9	1.67E-17	<0.51		
238	9	1.54E-15	<3.00		
262	9	3.56E-17	<1.78		
272	2	4.82E-17	5.549 ± 0.019	1750 ± 10	−28.9 ± 3.5
305	1	3.52E-17	<3.40		
329	9	6.91E-17	<2.29		
372	3	4.26E-17	<3.33		

Note. Columns: (1) BAT ID; (2) quality fit flag; (3) noise measured in the continuum in erg cm^{-2} s^{-1} Å^{-1}; (4), (5), and (6) Paβ flux (in units of 10^{-14} erg cm^{-2} s^{-1}), FWHM, and velocity shift, respectively. Values in column (4) preceded by "<" indicate upper limits. The upper limits on the broad-line fluxes have been computed using a FWHM = 4200 km s^{-1} (5).

(This table is available in its entirety in machine-readable form.)

Table A3
Broad-line Measurements of the Paα

BAT ID	Flag	Noise	Paα Flux	FWHM Paα (km s^{-1})	Δv Paα (km s^{-1})
(1)	(2)	(3)	(4)	(5)	(6)
7	2	1.52E-17	<10.65		
10	3	6.40E-18	1.69	8590 ± 61	−1000
80	4	1.89E-17	<3.41		
118	2	7.97E-18	<1.00		
238	2	1.52E-17	<1.91		
262	2	1.49E-17	<3.18		
272	4	6.93E-17	21.81	2419 ± 10	7.1 ± 2.5
305	2	1.25E-17	1.51 ± 0.013	1527 ± 27	31.2 ± 7.2
329	4	2.78E-17	<5.49		
372	3	9.86E-18	7.667 ± 0.024	11907 ± 32	−1000

Note. Columns: (1) BAT ID; (2) quality fit flag; (3) noise measured in the continuum in erg cm^{-2} s^{-1} Å^{-1}; (4), (5), and (6) Paα flux (in units of 10^{-14} erg cm^{-2} s^{-1}), FWHM, and velocity shift, respectively. Values in column (4) preceded by "<" indicate upper limits. The upper limits on the broad-line fluxes have been computed using a FWHM = 4200 km s^{-1}.

(This table is available in its entirety in machine-readable form.)

Table A4
Additional Gaussian Component of the He I in the Paγ Spectral Region

BAT ID	Flag	He I Flux	FWHM He I (km s^{-1})	Δv He I (km s^{-1})
(1)	(2)	(3)	(4)	(5)
372	3	2.86	1957	277
488	3	2.880 ± 0.059	1627.1 ± 0.03	−324.6 ± 6.2
577	3	0.31 ± 0.22	735 ± 186	−397 ± 16
698	3	0.13 ± 0.0020	856 ± 13	−993.3 ± 4.2
744	2	4.425 ± 0.062	3463 ± 44	238 ± 10
1064	2	7.97 ± 0.64	1212 ± 270	−364 ± 22
1079	2	7.432 ± 0.027	1008.8 ± 3.1	−287.3 ± 1.4

Note. Columns: (1) BAT ID; (2) quality fit flag (same as in Table A1); (3), (4), and (5) flux (in units of 10^{-14} erg cm^{-2} s^{-1}), FWHM, and velocity shift of the additional Gaussian component in the He I. These components were not used to measure the virial black hole masses.

Table A5
Additional Gaussian Component in the Paα Spectral Region

BAT ID	Flag	Paα Flux	H2 a Flux	H2 b Flux	FWHM Paα (km s^{-1})	FWHM H2 a (km s^{-1})	FWHM H2 b (km s^{-1})	Δv Paα (km s^{-1})	Δv H2 a (km s^{-1})	Δv H2 b (km s^{-1})
(1)	(2)	(3)	(4)	(5)	(6)	(7)	(8)	(9)	(10)	(11)
372	3	1.609 ± 0.014			3017.48 ± 0.05			593.3 ± 5.4		
1079	4	0.73 ± 0.24	2.599 ± 0.013	0.642 ± 0.011	299.45 ± 0.01	2974.68	29758	-148.25 ± 8.9	-453.62 ± 6.86	-999

Note. Columns: (1) BAT ID; (2) quality fit flag (same as in Table A3); (3), (6), (9) flux (in units of 10^{-14} erg cm^{-2} s^{-1}), FWHM, and velocity shift of the additional Gaussian component in the Paα, respectively; (4), (7), and (10) flux (in units of 10^{-14} erg cm^{-2} s^{-1}), FWHM, and velocity shift, of the H2 a, i.e., H2 λ18345; and (5), (8), and (11) flux (in units of 10^{-14} erg cm^{-2} s^{-1}), FWHM, and velocity shift of the H2 b, i.e., H2 λ18920. These additional Paα components were not used to measure the virial black hole masses.

Appendix B
f/f_0 Outliers

Table B1 presents all relevant physical properties of the targets showing reliable broad-line detections in the NIR with available stellar velocity dispersion measurements inside BASS. There are some targets showing an outlier nature in the f/f_0 distributions that have been omitted in our analysis. These sources are five in total, namely the following: IDs 670, 677, 1131, 1465, and 1470. The outliers are mostly (4/5) located above the 1:1 line in Figure 13, meaning that either the $M_{\mathrm{BH},\sigma_\star}$ is overestimated or the NIR BH mass is underestimated. The former case would indicate that the measured optical stellar velocity dispersion is unreliable for those sources, due to AGN contamination of the stellar absorption features, aperture effects, or host galaxy rotation contamination, while the latter case would happen if there is substantial obscuration along the line of sight, such that the highest velocity clouds of the BLR are not observable, being embedded in some obscuring medium. These four outliers are IDs 670, 1131, 1465, and 1470.

For BAT IDs 670, 1131, 1465, and 1470, the NIR+L_{X}-based BH mass is somehow underestimated. Those are part of the NIR DR2 (den Brok et al. 2022); those NIR spectra show only broad He I line, as Paα is located in a heavily affected telluric region, and Paβ is only detected, marginally, as a narrow line. All the other higher-order Paschen lines are missing as well. For ID 670, the broad He I transition might not be (fully) tracing the BLR, since a blueshifted outflow in the [O III] has been detected, with $v_{\max} = 1072^{+80}_{-990}$ km s^{-1} (Rojas et al. 2020).

For IDs 1131, 1465, and 1470 (Sy 1.8, 2, and 2, respectively), such information is not available since they were not part of the sample studied in Rojas et al. (2020). However, the optical BASS DR2 spectrum of BAT 1131 appears to have some ionized outflows in the [O III], as the residuals from a single Gaussian fit are rather prominent, blueshifted, and asymmetric. Therefore the broad component detected in the He I might not be describing the BLR. Additionally, this source, a Sy 1.8, is particularly AGN-dominated in the optical spectrum, making the stellar velocity dispersion measurement a bit tricky.

Finally, we note that for ID 1470 the Galactic extinction is fairly important, $E(B - V) = 0.48$ (corresponding to an $A_J = 0.354$ mag according to the IRSA dust database[49]); while for 1465, it is quite relevant, $E(B - V) = 3.03$ ($A_J = 2.150$ mag according to the IRSA database), probably affecting the NIR spectrum measurement.

One source is instead located below the 1:1 relation, at $\log f/f_0 < -1$, namely BAT 677. In this case, the NIR+L_{X}-based M(line) (e.g., $M(NIR) = 10^{7.140\pm0.023}\, M_\odot$) is about two orders of magnitude higher than the $\sigma_\star$-based BH mass estimate (e.g., $M_{\mathrm{BH},\sigma_\star} = 10^{5.47\pm0.29}\, M_\odot$). BAT 677 is part of the FIRE sample, and has a good Paβ fit (FWHM $= 2401 \pm 8$ km s^{-1}, fit quality 2). The $M_{\mathrm{BH},\sigma_\star}$ is computed from a rather small velocity dispersion measurement $\sigma_\star = 41 \pm 5$ km s^{-1} performed on the CaT region. We note that the BH–$\sigma_\star$ relation is not calibrated for $\sigma_\star < 65$ km s^{-1}; thus extrapolating to such low-velocity dispersion might introduce a higher error budget on the $M_{\mathrm{BH},\sigma_\star}$ estimation. We finally note that if instead of $\sigma_\star = 41$ we adopt $\sigma_\star = 68$ km s^{-1}, as measured from the Ca II and Mg I absorptions, the resulting $M_{\mathrm{BH},\sigma_\star}$ is about an order of magnitude higher ($M_{\mathrm{BH},\sigma_\star} = 10^{6.44\pm0.20}\, M_\odot$), and it is more consistent with the virial NIR+L_{X}-based estimate.

Therefore, for the former four sources, the NIR+L_{X}-based M(line) is not reliable, due to either the possible presence of outflows in ionized material disguised as BLR components (670, also possibly 1465 and 1470) or the high Galactic extinction in our line of sight (1465, 1470). For BAT 1131, both the $\sigma_\star$ and the NIR measurements are not trustable, for strong AGN contamination in the optical spectrum and for possible outflows in ionized material. Finally for BAT 677, the $M_{\mathrm{BH},\sigma_\star}$ is more uncertain to be located in the low-velocity dispersion extrapolation of the BH–$\sigma_\star$ scaling relation.

Table B1
Physical Properties of the Sample Having Both NIR-reliable Broad-line Detection and Optical Stellar Velocity Dispersion Measurements Available inside BASS

BAT ID	Sy class	FWHM (km s^{-1})				$\log M$(NIR) ($M_\odot$)	$\log f_{\mathrm{NIR}}$	$\log N_{\mathrm{H}}$ (cm^{-2})
		He I	Paβ	Paα	NIR			
(1)	(2)	(3)	(4)	(5)	(6)	(7)	(8)	(9)
10	1.9	5906 ± 336			5906 ± 336	8.827 ± 0.054	0.91 ± 0.15	21.98
53	2	3260 ± 188			3260 ± 188	7.910 ± 0.055	0.705 ± 0.092	23.54
63	2		1429 ± 36		1429 ± 36	6.664 ± 0.032	1.42 ± 0.11	23.30
72	1.9	2347 ± 76	6673 ± 183		2975 ± 70	7.797 ± 0.031	1.059 ± 0.068	22.01
73	1.2	2226 ± 30	5960 ± 80		2690 ± 28	8.020 ± 0.025	1.43 ± 0.10	20.00
193	2	3351 ± 271			3351 ± 271	7.904 ± 0.074	1.77 ± 0.10	24.32
202	1.9	6122 ± 203			6122 ± 203	8.728 ± 0.037	0.457 ± 0.065	23.03
217	2	4634 ± 128			4634 ± 128	8.283 ± 0.033	1.141 ± 0.063	22.89
218	2		1750 ± 68		1750 ± 68	7.477 ± 0.041	-0.10 ± 0.16	23.84
246	1.9	5355 ± 155			5355 ± 155	8.582 ± 0.034	0.522 ± 0.064	22.18

Note. Columns are as follows: (1) BAT ID; (2) optical Seyfert classification; (3)–(6) near-infrared broad-line measurements, from either BASS DR1 (Lamperti et al. 2017), DR2 (den Brok et al. 2022), or from this work, i.e., FIRE spectra; (7) logarithm of the mixed NIR+L_{X}-based BH mass, calculated using the FWHM(NIR); (8) logarithm of the virial factor computed as the ratio of the $\sigma_\star$-based BH mass with velocity dispersions from the BASS DR2 (either from Koss et al. 2022, or T. Caglar et al. 2022, in preparation) and $M(NIR)$; (9) column density derived from X-ray spectral fitting (Ricci et al. 2017a). Upper limits on the X-ray columns are denoted with $<$.

(This table is available in its entirety in machine-readable form.)

ORCID iDs

Federica Ricci ⓘ https://orcid.org/0000-0001-5742-5980
Ezequiel Treister ⓘ https://orcid.org/0000-0001-7568-6412
Franz E. Bauer ⓘ https://orcid.org/0000-0002-8686-8737
Julian E. Mejía-Restrepo ⓘ https://orcid.org/0000-0001-8450-7463
Michael J. Koss ⓘ https://orcid.org/0000-0002-7998-9581
Jakob S. den Brok ⓘ https://orcid.org/0000-0002-8760-6157
Mislav Baloković ⓘ https://orcid.org/0000-0003-0476-6647
Rudolf Bär ⓘ https://orcid.org/0000-0001-5481-8607
Patricia Bessiere ⓘ https://orcid.org/0000-0002-0205-5940
Turgay Caglar ⓘ https://orcid.org/0000-0002-9144-2255
Fiona Harrison ⓘ https://orcid.org/0000-0003-2992-8024
Kohei Ichikawa ⓘ https://orcid.org/0000-0002-4377-903X
Darshan Kakkad ⓘ https://orcid.org/0000-0002-2603-2639
Isabella Lamperti ⓘ https://orcid.org/0000-0003-3336-5498
Richard Mushotzky ⓘ https://orcid.org/0000-0002-7962-5446
Kyuseok Oh ⓘ https://orcid.org/0000-0002-5037-951X
Meredith C. Powell ⓘ https://orcid.org/0000-0003-2284-8603
George C. Privon ⓘ https://orcid.org/0000-0003-3474-1125
Claudio Ricci ⓘ https://orcid.org/0000-0001-5231-2645
Rogerio Riffel ⓘ https://orcid.org/0000-0002-1321-1320
Alejandra F. Rojas ⓘ https://orcid.org/0000-0003-0006-8681
Eleonora Sani ⓘ https://orcid.org/0000-0002-3140-4070
Krista L. Smith ⓘ https://orcid.org/0000-0001-5785-7038
Daniel Stern ⓘ https://orcid.org/0000-0003-2686-9241
Benny Trakhtenbrot ⓘ https://orcid.org/0000-0002-3683-7297
C. Megan Urry ⓘ https://orcid.org/0000-0002-0745-9792
Sylvain Veilleux ⓘ https://orcid.org/0000-0002-3158-6820

References

Baldassare, V. F., Reines, A. E., Gallo, E., & Greene, J. E. 2017, ApJ, 836, 20
Baldassare, V. F., Reines, A. E., Gallo, E., et al. 2016, ApJ, 829, 57
Barthelmy, S. D. 2000, Proc. SPIE, 4140, 50
Batiste, M., Bentz, M. C., Raimundo, S. I., Vestergaard, M., & Onken, C. A. 2017, ApJL, 838, L10
Baumgartner, W. H., Tueller, J., Markwardt, C. B., et al. 2013, ApJS, 207, 19
Bennert, V. N., Auger, M. W., Treu, T., Woo, J.-H., & Malkan, M. A. 2011, ApJ, 726, 59
Bentz, M. C., Denney, K. D., Grier, C. J., et al. 2013, ApJ, 767, 149
Bentz, M. C., Peterson, B. M., Pogge, R. W., Vestergaard, M., & Onken, C. A. 2006, ApJ, 644, 133
Bentz, M. C., Walsh, J. L., Barth, A. J., et al. 2009, ApJ, 705, 199
Bernardi, M., Sheth, R. K., Tundo, E., & Hyde, J. B. 2007, ApJ, 660, 267
Blandford, R. D., & McKee, C. F. 1982, ApJ, 255, 419
Bongiorno, A., Maiolino, R., Brusa, M., et al. 2014, MNRAS, 443, 2077
Burtscher, L., Davies, R. I., Graciá-Carpio, J., et al. 2016, A&A, 586, A28
Caglar, T., Burtscher, L., Brandl, B., et al. 2020, A&A, 634, A114
Cai, H.-B., Shu, X.-W., Zheng, Z.-Y., & Wang, J.-X. 2010, RAA, 10, 427
Calzetti, D., Armus, L., Bohlin, R. C., et al. 2000, ApJ, 533, 682
Chilingarian, I. V., Katkov, I. Y., Zolotukhin, I. Y., et al. 2018, ApJ, 863, 1
Collin, S., Kawaguchi, T., Peterson, B. M., & Vestergaard, M. 2006, A&A, 456, 75
de Nicola, S., Marconi, A., & Longo, G. 2019, MNRAS, 490, 600
Decarli, R., Labita, M., Treves, A., & Falomo, R. 2008, MNRAS, 387, 1237
den Brok, J., Koss, M. J., Trakhtenbrot, B., et al. 2022, ApJS, 261, 7
Domínguez, A., Siana, B., Henry, A. L., et al. 2013, ApJ, 763, 145
Falcón-Barroso, J., Lyubenova, M., van de Ven, G., et al. 2017, A&A, 597, A48
Gagné, J., Lambrides, E., Faherty, J. K., & Simcoe, R. 2015, FireHose_v2: Firehose v2.0, Zenodo, doi:10.5281/zenodo.18775
Gandhi, P., Hönig, S. F., & Kishimoto, M. 2015, ApJ, 812, 113
Ginsburg, A., & Mirocha, J. 2011, PySpecKit: Python Spectroscopic Toolkit, Astrophysics Source Code Library, ascl:1109.001
Glikman, E., Helfand, D. J., & White, R. L. 2006, ApJ, 640, 579
Goodrich, R. W., Veilleux, S., & Hill, G. J. 1994, ApJ, 422, 521

Graham, A. W. 2008, ApJ, 680, 143
Gravity Collaboration, Amorim, A., Bauböck, M., et al. 2020, A&A, 643, A154
Gravity Collaboration, Sturm, E., Dexter, J., et al. 2018, Nature, 563, 657
Greene, J. E., & Ho, L. C. 2004, ApJ, 610, 722
Greene, J. E., & Ho, L. C. 2005, ApJ, 630, 122
Greene, J. E., & Ho, L. C. 2007, ApJ, 670, 92
Grier, C. J., Martini, P., Watson, L. C., et al. 2013, ApJ, 773, 90
Grier, C. J., Pancoast, A., Barth, A. J., et al. 2017, ApJ, 849, 146
Gültekin, K., Richstone, D. O., Gebhardt, K., et al. 2009, ApJ, 698, 198
Güver, T., & Özel, F. 2009, MNRAS, 400, 2050
Har, C. E., Bennert, V. N., Auger, M. W., et al. 2012, ApJS, 201, 29
Ho, L. C., & Kim, M. 2014, ApJ, 789, 17
Inayoshi, K., Visbal, E., & Haiman, Z. 2020, ARA&A, 58, 27
Jarrett, T. H., Chester, T., Cutri, R., et al. 2000, AJ, 119, 2498
Kang, W.-Y., Woo, J.-H., Schulze, A., et al. 2013, ApJ, 767, 26
Kelly, B. C. 2007, ApJ, 665, 1489
Kim, D., Im, M., & Kim, M. 2010, ApJ, 724, 386
Kormendy, J., & Ho, L. C. 2013, ARA&A, 51, 511
Kormendy, J., & Richstone, D. 1995, ARA&A, 33, 581
Koss, M., Mushotzky, R., Veilleux, S., et al. 2011, ApJ, 739, 57
Koss, M., Mushotzky, R., Veilleux, S., & Winter, L. 2010, ApJL, 716, L125
Koss, M., Trakhtenbrot, B., Ricci, C., et al. 2017, ApJ, 850, 74
Koss, M. J., Assef, R., Baloković, M., et al. 2016, ApJ, 825, 85
Koss, M. J., Ricci, C., Trakhtenbrot, B., et al. 2022, ApJS, 261, 2
La Franca, F., Onori, F., Ricci, F., et al. 2015, MNRAS, 449, 1526
Lamperti, I., Koss, M., Trakhtenbrot, B., et al. 2017, MNRAS, 467, 540
Landt, H., Bentz, M. C., Ward, M. J., et al. 2008, ApJS, 174, 282
Li, Y.-R., Songsheng, Y.-Y., Qiu, J., et al. 2018, ApJ, 869, 137
Liu, H., Luo, B., Brandt, W. N., et al. 2021, ApJ, 910, 103
Lusso, E., Comastri, A., Vignali, C., et al. 2010, A&A, 512, A34
Lusso, E., Risaliti, G., Nardini, E., et al. 2020, A&A, 642, A150
Maiolino, R., Marconi, A., Salvati, M., et al. 2001, A&A, 365, 28
Maiolino, R., Risaliti, G., Salvati, M., et al. 2010, A&A, 517, A47
Markowitz, A. G., Krumpe, M., & Nikutta, R. 2014, MNRAS, 439, 1403
Marsden, C., Shankar, F., Ginolfi, M., & Zubovas, K. 2020, FrP, 8, 61
Martínez-Palomera, J., Lira, P., Bhalla-Ladd, I., Förster, F., & Plotkin, R. M. 2020, ApJ, 889, 113
Masini, A., Comastri, A., Baloković, M., et al. 2016, A&A, 589, A59
Mason, R. E., Rodríguez-Ardila, A., Martins, L., et al. 2015, ApJS, 217, 13
McConnell, N. J., & Ma, C.-P. 2013, ApJ, 764, 184
McLure, R. J., & Jarvis, M. J. 2002, MNRAS, 337, 109
Mejía-Restrepo, J. E., Lira, P., Netzer, H., Trakhtenbrot, B., & Capellupo, D. M. 2018, NatAs, 2, 63
Mejía-Restrepo, J., Koss, M. J., Trakhtenbrot, B., et al. 2022, ApJS, 261, 5
Mezcua, M. 2017, IJMPD, 26, 1730021
Mezcua, M., Civano, F., Marchesi, S., et al. 2018, MNRAS, 478, 2576
Moran, E. C., Shahinyan, K., Sugarman, H. R., Vélez, D. O., & Eracleous, M. 2014, AJ, 148, 136
Nowak, M. A., Neilsen, J., Markoff, S. B., et al. 2012, ApJ, 759, 95
Oh, K., Koss, M., Markwardt, C. B., et al. 2018, ApJS, 235, 4
Onken, C. A., Ferrarese, L., Merritt, D., et al. 2004, ApJ, 615, 645
Onori, F., La Franca, F., Ricci, F., et al. 2017a, MNRAS, 464, 1783
Onori, F., Ricci, F., La Franca, F., et al. 2017b, MNRAS, 468, L97
Oohama, N., Okamura, S., Fukugita, M., Yasuda, N., & Nakamura, O. 2009, ApJ, 705, 245
Osterbrock, D. E. 1981, ApJ, 249, 462
Osterbrock, D. E., & Ferland, G. J. 2006, Astrophysics of Gaseous Nebulae and Active Galactic Nuclei (Sausalito, CA: Univ. Science Books)
Pacucci, F., Loeb, A., Mezcua, M., & Martín-Navarro, I. 2018, ApJL, 864, L6
Pancoast, A., Barth, A. J., Horne, K., et al. 2018, ApJ, 856, 108
Pancoast, A., Brewer, B. J., Treu, T., et al. 2014, MNRAS, 445, 3073
Predehl, P., & Schmitt, J. H. M. M. 1995, A&A, 500, 459
Privon, G. C., Ricci, C., Aalto, S., et al. 2020, ApJ, 893, 149
Ramos Almeida, C., & Ricci, C. 2017, NatAs, 1, 679
Reines, A. E., Greene, J. E., & Geha, M. 2013, ApJ, 775, 116
Reines, A. E., & Volonteri, M. 2015, ApJ, 813, 82
Ricci, C., Bauer, F. E., Arevalo, P., et al. 2016, ApJ, 820, 5
Ricci, C., Trakhtenbrot, B., Koss, M. J., et al. 2017a, ApJS, 233, 17
Ricci, C., Ueda, Y., Koss, M. J., et al. 2015, ApJL, 815, L13
Ricci, F., La Franca, F., Marconi, A., et al. 2017b, MNRAS, 471, L41
Ricci, F., La Franca, F., Onori, F., & Bianchi, S. 2017c, A&A, 598, A51
Riffel, R., Rodríguez-Ardila, A., Aleman, I., et al. 2013, MNRAS, 430, 2002
Riffel, R., Rodríguez-Ardila, A., & Pastoriza, M. G. 2006, A&A, 457, 61
Riffel, R. A., Ho, L. C., Mason, R., et al. 2015, MNRAS, 446, 2823

Risaliti, G., Elvis, M., Fabbiano, G., et al. 2007, ApJL, 659, L111
Risaliti, G., Nardini, E., Salvati, M., et al. 2011, MNRAS, 410, 1027
Rojas, A. F., Sani, E., Gavignaud, I., et al. 2020, MNRAS, 491, 5867
Ryan-Weber, E. V., Webster, R. L., & Staveley-Smith, L. 2003, MNRAS, 343, 1195
Saglia, R. P., Opitsch, M., Erwin, P., et al. 2016, ApJ, 818, 47
Sahu, N., Graham, A. W., & Davis, B. L. 2019, ApJ, 887, 10
Schlafly, E. F., & Finkbeiner, D. P. 2011, ApJ, 737, 103
Schnorr-Müller, A., Davies, R. I., Korista, K. T., et al. 2016, MNRAS, 462, 3570
Sexton, R. O., Canalizo, G., Hiner, K. D., et al. 2019, ApJ, 878, 101
Shankar, F., Bernardi, M., Richardson, K., et al. 2019, MNRAS, 485 1278
Shankar, F., Bernardi, M., Sheth, R. K., et al. 2016, MNRAS, 460, 3119
Shen, Y. 2013, BASI, 41, 61
Shen, Y., Brandt, W. N., Richards, G. T., et al. 2016, ApJ, 831, 7
Shen, Y., Greene, J. E., Ho, L. C., et al. 2015, ApJ, 805, 96
Shen, Y., & Ho, L. C. 2014, Nature, 513, 210
Shimizu, T. T., Davies, R. I., Koss, M., et al. 2018, ApJ, 856, 154

Simcoe, R. A., Burgasser, A. J., Bernstein, R. A., et al. 2008, Proc. SPIE, 7014, 70140U
Smette, A., Sana, H., Noll, S., et al. 2015, A&A, 576, A77
Smith, K. L., Koss, M., & Mushotzky, R. F. 2014, ApJ, 794, 112
Soifer, B. T., Charmandaris, V., Brandl, B. R., et al. 2004, ApJS, 154, 151
Treister, E., Schawinski, K., Volonteri, M., & Natarajan, P. 2013, ApJ, 778, 130
Treister, E., Virani, S., Gawiser, E., et al. 2009, ApJ, 693, 1713
van den Bosch, R. C. E. 2016, ApJ, 831, 134
Veilleux, S. 2002, in ASP Conf. Ser. 284, IAU Coll. 184: AGN Surveys, ed. R. F. Green, E. Y. Khachikian, & D. B. Sanders (San Francisco, CA: ASP), 111
Veilleux, S., Goodrich, R. W., & Hill, G. J. 1997, ApJ, 477, 631
Vestergaard, M., & Peterson, B. M. 2006, ApJ, 641, 689
Volonteri, M., Lodato, G., & Natarajan, P. 2008, MNRAS, 383, 1079
Williams, P. R., Pancoast, A., Treu, T., et al. 2018, ApJ, 866, 75
Woo, J.-H., Schulze, A., Park, D., et al. 2013, ApJ, 772, 49
Yu, L.-M., Bian, W.-H., Wang, C., Zhao, B.-X., & Ge, X. 2019, MNRAS, 488, 1519
Zaino, A., Bianchi, S., Marinucci, A., et al. 2020, MNRAS, 492, 3872

26